Article

Spatial organization of translation and translational repression in two phases of germ granules

Anne Ramat [1,2] ✉, Ali Haidar [1,2], Céline Garret[1] & Martine Simonelig [1] ✉

Most RNA-protein condensates are composed of heterogeneous immiscible phases. However, how this multiphase organization contributes to their biological functions remains largely unexplored. *Drosophila* germ granules, a class of RNA-protein condensates, are the site of mRNA storage and translational activation. Here, using super-resolution microscopy and single-molecule imaging approaches, we show that germ granules have a biphasic organization and that translation occurs in the outer phase and at the surface of the granules. The localization, directionality, and compaction of mRNAs within the granule depend on their translation status, translated mRNAs being enriched in the outer phase with their 5′end oriented towards the surface. Translation is strongly reduced when germ granule biphasic organization is lost. These findings reveal the intimate links between the architecture of RNA-protein condensates and the organization of their different functions, highlighting the functional compartmentalization of these condensates.

Membraneless biomolecular condensates have recently emerged as fundamental in cell biology favoring the coordination and efficiency of biochemical reactions by concentrating substrates and enzymes in a common space. Their assembly depends on a demixing process that involves multivalent interactions between proteins and nucleic acids once their concentrations reach a specific threshold[1]. RNA-protein (RNP) condensates, also called RNA granules, exist in both the nucleus and cytoplasm and are linked to most aspects of RNA biology[2,3]. Yet, although the biophysical properties and assembly mechanisms of RNP condensates have been deeply investigated, the biological functions of most of them remain poorly understood[4–6]. Super-resolution microscopy approaches have revealed that many RNP condensates are not homogeneous but rather composed of multiple immiscible phases, reflected by a heterogeneous distribution of RNA and/or RNA binding proteins[3,7]. The best understood example of this phenomenon is the nucleolus in which three nested phases are linked to three different steps of ribosome biogenesis[8–10]. For other RNP condensates, the functional relevance of their higher-order organization remains elusive.

Germ granules are evolutionary conserved germline specific RNP condensates that instruct germ cell fate through mRNA regulation[11,12].

They are hubs for mRNA storage and translational control. *Drosophila* embryonic germ granules contain ≈200 different maternal mRNAs[13,14] as well as four main proteins: the germ granule inducer Oskar (Osk), Vasa, an RNA helicase homolog of human DDX4, the scaffold protein Tudor (Tud) and Aubergine (Aub), an Argonaute protein of the PIWI clade[15]. *Drosophila* germ granules display both liquid-like and hydrogel-like properties, mRNA representing a stable component of the granule[16,17]. Multiple copies of the same mRNA molecules are grouped together in homotypic clusters[18,19], although the function behind this organization is still unknown. In several species, germ granules have a multiphase architecture[20,21], and understanding the relationships between this organization and germ granule functions is attracting a growing interest. In particular, although the function of germ granules in the storage of repressed mRNAs is well described, whether they are also sites for translational activation remains an open question. In *C. elegans*, translational activation of germ granule mRNAs coincides with their relocalization to the cytoplasm[22,23]. In *Drosophila* embryos, translation of germ granule mRNAs follows a tight temporal sequence[13], implying that germ granules achieve temporal translational control by coordinating concomitant translational repression

[1]Institute of Human Genetics, Université de Montpellier, CNRS, Montpellier, France. [2]These authors contributed equally: Anne Ramat, Ali Haidar.
✉e-mail: Anne.Ramat@igh.cnrs.fr; Martine.Simonelig@igh.cnrs.fr

of some mRNAs and activation of others. We took advantage of this outstanding property to determine how these opposite functions are compartmentalized within germ granules and address the relationships between architecture and biological functions of RNP condensates.

Results

Drosophila germ granules have a biphasic organization

Due to the small size of germ granules, ranging from 200 to 500 nm[24], we used super-resolution 2D Stimulated Emission Depletion (STED) microscopy to characterize the distribution of germ granule main protein components. We set up a method to slice and expose the posterior pole of embryos to the objective, in order to reduce the distance between the sample and the objective and get optimal resolution (Supplementary Fig. 1a–c and Supplementary Note). All four main components of germ granules were enriched in the outer most part of the granule that we termed outer phase or shell (Fig. 1a) and they colocalized as quantified using the Pearson Correlation Coefficient (PCC(Costes)) (Supplementary Fig. 1d). This organization was reminiscent of the germ granule structure observed previously by electron microscopy, showing an electron dense periphery and lucid center[25,26]. STED microscopy requires the use of an antibody to get a signal that stands the depletion. To rule out that the observed pattern was the consequence of poor antibody penetration within the granule, we used AiryScan and 3D-OMX microscopy to visualize the localization of GFP-tagged versions of Aub, Vasa, and Tud using GFP fluorescence. The same enrichment was observed in the shell (Fig. 1b, Supplementary Fig. 1c). Furthermore, GFP-Aub and Vasa-tdTomato visualized using 3D-OMX without antibody staining also colocalized in the shell of germ granules (Fig. 1c). GFP-Aub enrichment in the outer phase was visible in 3D (Supplementary Fig. 1e), consistent with previous observations based on electron microscopy of ultra-thin sections that led to propose a hollow sphere morphology of germ granules[26]. To further confirm that a substantial proportion of germ granules in early embryos had this hollow morphology, we visualized germ granules in two consecutive serial sections using transmission electron microscopy. This approach showed that of 16 germ granules present on both sections, 15 (94%) were visualized as hollow in at least one section, whereas of 11 granules present on a single section, only two had a hollow center (Supplementary Fig. 1f, g). These data revealed the importance of imaging through the granule volume when using ultra-thin sections (70 nm) to access granule morphology, as reported previously[26]. Of note, enrichment of germ granule major proteins in the outer phase was not described in previous studies based on structured illumination microscopy (SIM)[17–19]. We believe that this difference comes from the higher resolution (60 ± 12 nm, see "Methods") reached using STED microscopy combined with our slicing method (Supplementary Fig. 1c), as compared to SIM (typically 100 nm). Further studies will be needed to fully resolve this discrepancy. Using STED acquisitions and Osk protein as a marker, we applied a Laplacian of Gaussian filter to define the edges of germ granule outer and inner phases (see "Methods") and measured the size of germ granules and their outer phase. Germ granule diameters ranged from 110 to 570 nm with a mean of 308 ± 86 nm (Fig. 1d), and the thickness of the outer phase ranged from 54 to 224 nm with a mean of 104 ± 25 nm (Fig. 1e). We conclude that germ granules have a multiphase structure, with main protein components enriched in the outer phase.

Aub is required for the biphasic architecture and maintenance of germ granules

Aub binds germ granule mRNAs through base-pairing with piRNAs and is a major actor of their recruitment to germ granules[14,27,28]. Through this function, Aub is expected to play an important role in maintaining the RNA content of germ granules. We thus addressed the contribution

of mRNAs to germ granule biphasic organization by analyzing germ granule architecture in the absence of Aub. We used a specific genetic set up to visualize germ granules in *aub* mutant embryos. Indeed, due to early developmental defects during oogenesis in *aub* mutants, Osk protein is not produced at the posterior pole, and germ granules do not form in these mutants[29]. However, Osk does accumulate at the anterior pole of embryos following recruitment of *osk* mRNA to the anterior pole, even in the absence of Aub[27,30]. In this context, germ granule mRNAs localize very poorly to the anterior pole, consistent with the role of Aub in mRNA recruitment to germ granules[27]. Using STED imaging and Osk as a marker, we found that germ granules produced at the anterior pole when *osk* mRNA was delocalized had a similar biphasic organization as those present at the posterior pole of wild-type embryos (Supplementary Fig. 2a). In contrast, in *aub* mutant embryos, germ granule architecture was severely affected, with the disappearance of their biphasic organization and a diameter reduced to 158 ± 37 nm, instead of 324 ± 66 nm in the *aub*[+] background (Supplementary Fig. 2b, c). In line with Aub function in mRNA recruitment to germ granules, *nos* mRNA was not found in these germ granules using single molecule Fluorescent In Situ Hybridization (smFISH) and STED imaging (Supplementary Fig. 2d). In addition, these germ granules disappeared altogether in 79.3% of embryos ($n = 53$) after 2.5 h of development, while they were maintained in the *aub*[+] background (100% of embryos, $n = 50$).

These data demonstrate the essential contribution of Aub to germ granule biphasic organization and maintenance, in part through its ability to recruit mRNAs.

nos mRNA translation occurs in the outer phase and at the immediate periphery of germ granules

To understand how germ granule mRNA translation integrates within germ granule architecture, we used the Suntag method that allows the visualization of ongoing translation[31–35], to monitor *nos* mRNA translation. Briefly, the binding of single-chain antibodies fused to GFP (scFv-GFP) on an array of GCN4-based epitope (called Suntag) placed downstream of the start codon of the mRNA of interest allows the visualization of nascent peptides by creating bright GFP spots above background whose intensity reflects translation efficiency (Fig. 2a). Translating mRNAs are detected either by the MS2/MCP system[36] or smFISH[37]. We inserted an array of 12 Suntag repeats after *nos* initiation codon (Supplementary Fig. 3a) in a genomic construct known to rescue *nos* RNA null mutant (*nos*[BN]) phenotypes[38]. We first recorded the efficiency of *suntag-nos* mRNA localization to the germ plasm, the cytoplasm containing germ granules at the posterior pole of embryos, by measuring *suntag* smFISH fluorescence intensity at the posterior pole and in whole embryos expressing *suntag-nos* and comparing this quantification to that of *nos* smFISH fluorescence intensity in wild-type embryos. While 3.8% of *nos* mRNA localized to the posterior pole in wild-type embryos as previously reported[18,39], 2.15% of *suntag-nos* mRNA localized to the posterior pole (Supplementary Fig. 3b), indicating a reduced recruitment of the chimeric *suntag-nos* mRNA to the germ plasm. Nonetheless, the *suntag-nos* construct was able to rescue *nos*[BN] embryonic lethality (*nos*[BN]: 100% embryonic lethality, *suntag-nos/+; nos*[BN]: 48.7% embryonic lethality, $n > 100$ embryos), showing that the regulation of *suntag-nos* mRNA, including its level of localization and translational control allowed embryonic development.

Using confocal microscopy, we found that *suntag-nos* embryos containing maternally-provided scFv-GFP (*nos-scFv-GFP*[40]) showed bright GFP foci at the posterior pole as expected for Nos protein production site (Fig. 2b). To determine whether these GFP foci reflected *suntag-nos* mRNA translation, first, we analyzed their colocalization with cognate mRNA using smFISH probes directed against the *suntag* sequence, and STED super-resolution imaging (Fig. 2c). We quantified that 70% of scFv-GFP foci colocalized with *suntag* mRNA (Fig. 2e), revealing translating mRNAs. Second, we showed that these scFv-GFP
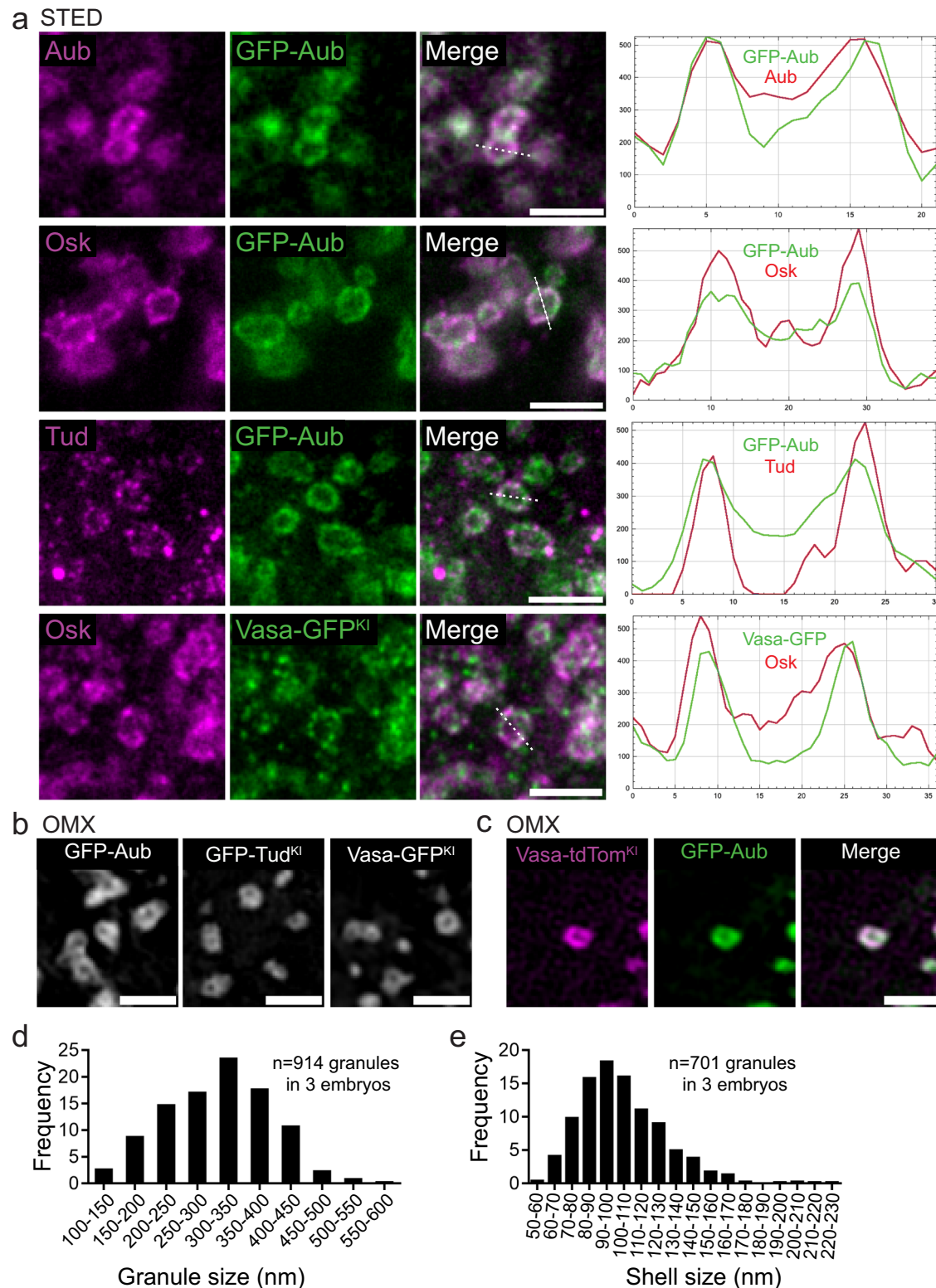
Fig. 1 | *Drosophila* germ granules have a biphasic organization. a STED imaging of germ granule main components. Immunostaining of *UASp-GFP-Aub; nos-Gal4* or *vasa-GFP^KI* embryos with anti-Aub (magenta), anti-Osk (magenta), anti-Tud (magenta), and anti-GFP (green) to visualize GFP-Aub or Vasa-GFP. Fluorescence intensity (right) was measured along the path marked with a white dashed line and intensity profiles of each channel are shown on the graph. **b** 3D-OMX imaging of *UASp-GFP-Aub; nos-Gal4* (left), *GFP-Tud^KI* (middle), *Vasa-GFP^KI* (right) in which GFP was directly recorded without antibody staining. **c** 3D-OMX imaging of *UASp-GFP-Aub/ vasa-tdTom^KI; nos-Gal4/+* embryos in which GFP and tdTomato were directly recorded without antibody staining. **d**, **e** Measurement of germ granule size (**d**) and outer phase size (**e**) from wild-type embryos immunostained with Osk antibody and imaged using STED microscopy. Scale bars: 1 µm. Source data are provided as a Source Data file.
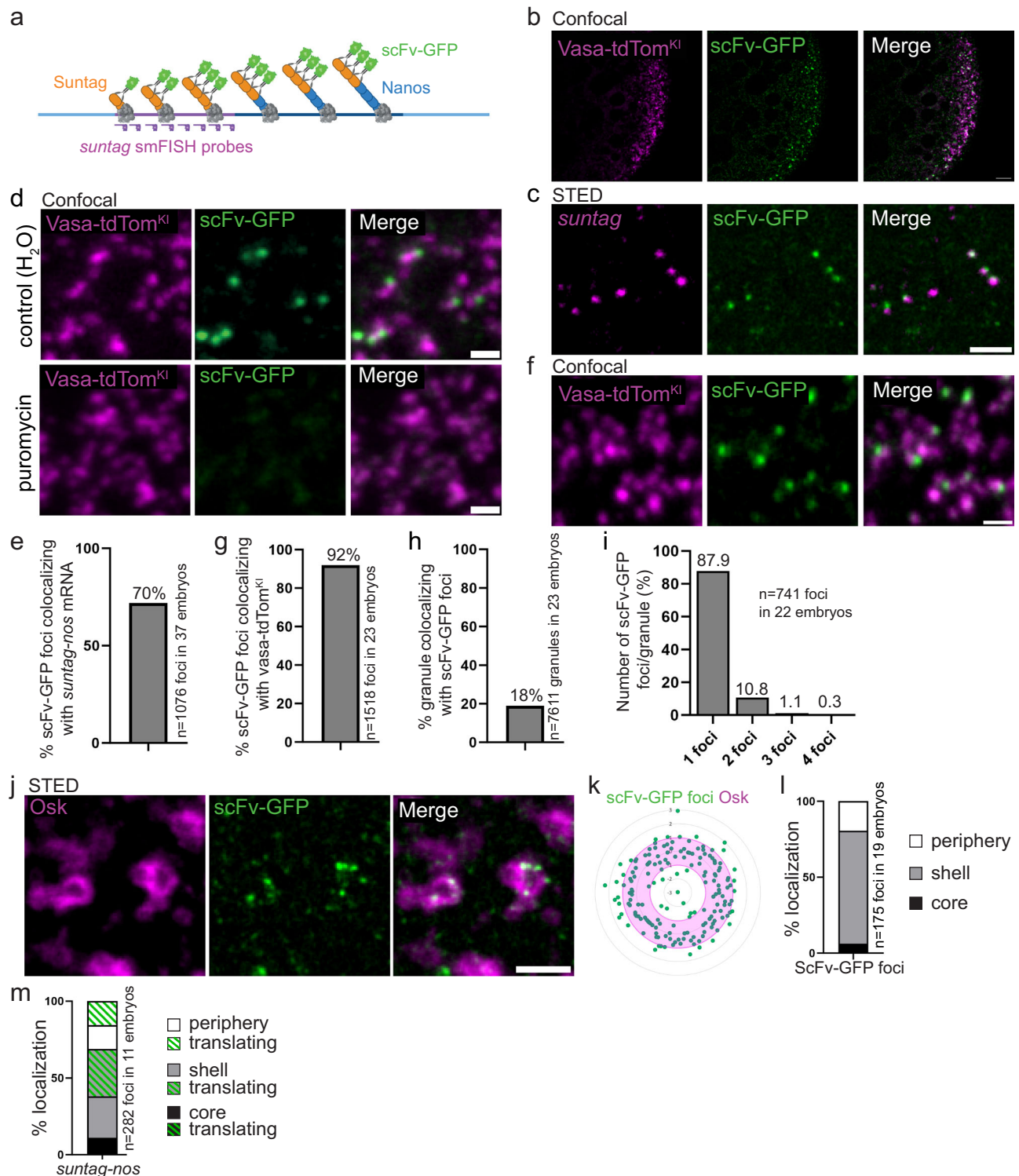
foci disappeared upon treatment of embryos with puromycin that releases translating ribosomes[31] (Fig. 2d), confirming that scFv-GFP foci corresponded to translation sites or accumulation of freshly produced Suntag-Nos protein. We next addressed the localization of scFv-GFP foci in relation with germ granules marked with Vasa-tdTomato. Confocal imaging revealed that 92% of scFv-GFP foci colocalized with or over-lapped germ granules (Fig. 2f, g). This suggested that *suntag-nos* mRNA translation occurred exclusively at germ granules and not in the inter-granular space. To confirm this result, we performed immuno-smFISH to visualize *suntag-nos* mRNA, scFv-GFP foci, and germ granules marked with Osk (Supplementary Fig. 3c). Quantification of confocal images

(see "Methods") showed that all (99.85%) translation events were restricted to the germ plasm and adjacent or colocalizing with germ granules (Supplementary Fig. 3c). Therefore *suntag-nos* mRNA transla-tion occurred specifically at germ granules.

We quantified that 18% of germ granules marked with Vasa-tdTomato colocalized with scFv-GFP foci, and were thus translating *suntag-nos* mRNA (Fig. 2f, h). Most translating germ granules (87.9%) had a single scFv-GFP foci, but up to four scFv-GFP foci could be visualized per granule (Fig. 2i). However, it should be noted that these numbers would be expected to be higher for endogenous *nos* mRNA translation as a lower level of *suntag-nos* localized to the germ plasm

Fig. 2 | Visualization of *nos* mRNA translation at germ granules using Suntag. **a** Principle of the Suntag technique to visualize *nos* mRNA translation. Blue lines: *nos* mRNA (light blue: UTRs, dark blue: CDS). Purple line: Suntag array. The polysomes are in grey. The Suntag and Nos nascent peptides are in orange and blue, respectively. The scFv-GFP antibody (green) binds the Suntag peptide. *suntag* smFISH probes are in purple. Created on Biorender.com. **b** Confocal images of *vasa-tdTom^Kt/nos-suntag-nos; nos-scFv-GFP/+* embryos. Vasa-tdTomato (magenta) and scFv-GFP (green) fluorescence were directly recorded without antibody staining. **c** STED images of immuno-smFISH of *nos-suntag-nos/+; nos-scFv-GFP/+* embryos with anti-GFP nanobody (green) to detect scFv-GFP and *suntag* smFISH probes (magenta). **d** Fluorescent confocal images of *vasa-tdTom^Kt/nos-suntag-nos; nos-scFv-GFP/+* permeabilized embryos without (top) and with puromycin treatment (bottom). Vasa-tdTomato (magenta) and scFv-GFP (green) fluorescence were directly recorded. **e** Percentage of scFv-GFP foci colocalizing with *suntag-nos* mRNA from images as in (**c**). **f** Close-up view of fluorescent confocal images of *vasa-tdTom^Kt/nos-suntag-nos; nos-scFv-GFP/+* embryos showing scFv foci with germ granules. Vasa-tdTomato (magenta) and scFv-GFP (green) fluorescence were directly recorded. **g** Percentage of scFv-GFP foci colocalizing with germ granules marked with Vasa-tdTom from images as in (**f**). **h** Percentage of germ granules marked with Vasa-tdTom colocalizing with scFv-GFP foci, i.e., undergoing translation, from images as in (**f**). **i** Quantification of the number of scFv-GFP foci per granule from images as in (**f**). **j** STED imaging of *nos-suntag-nos/+; nos-scFv-GFP/+* embryos immunostained with anti-Osk antibody (magenta) and anti-GFP nanobody (green) to reveal scFv-GFP. **k, l** Quantification of svFv-GFP foci localization within the germ granule biphasic structure from STED images as in (**j**). Radar plot of the relative distance of scFv-GFP foci (green dots) within Osk immunostaining (magenta). The granule shell is in pink (**k**). Percentage of scFv-GFP foci localized in the core (black), in and at the surface of the shell (grey), and at the immediate granule periphery (white) (**l**). **m** Percentage of *suntag-nos* mRNA foci localized in the core (black), in and at the surface of the shell (grey), and at the immediate granule periphery (white). The green dashed part in each category represents the proportion of *suntag-nos* foci undergoing translation (i.e., colocalizing with scFv-GFP) from images as in Supplementary Fig. 3e, f. Scale bars: 5 μm in (**b**), 1 μm in (**c–e**, **j**). Source data are provided as a Source Data file. **a** Created with BioRender.com released under a Creative Commons Attribution-NonCommercial-NoDerivs 4.0 International license.

(Supplementary Fig. 3b), and we quantified using FISH-quant[41] a lower number of *suntag-nos* mRNA molecules per cluster compared to that of endogenous *nos* mRNA[42] (Supplementary Fig. 3d).

We next used STED super-resolution microscopy to record the localization of translation events within germ granules (Fig. 2j). We found that most scFv-GFP foci localized in the outer phase and at the granule immediate periphery (74.3% and 19.4%, respectively), with only 6.3% localizing in the inner phase of the granule (Fig. 2j-l). We performed immuno-smFISH to visualize scFv-GFP, *suntag-nos* mRNA, and germ granule marked by Osk, using STED microscopy. We observed that *suntag-nos* mRNA and scFv-GFP translation foci were not organized in a specific order within the outer phase, scFv-GFP foci appearing either at the same level or in a more internal or more external position than *suntag-nos* mRNA within the outer phase (Supplementary Fig. 3e). Importantly, when *suntag-nos* mRNA was detected in the inner phase or core of the granule, it was not associated with scFv-GFP foci (Supplementary Fig. 3f, 100% *n* = 31 granules), indicating a lack of translation. Using this triple staining and STED microscopy, we recorded the localization of translating (associated with scFv-GFP foci) and non-translating *suntag-nos* mRNA within germ granules and found that among the 11% of *suntag-nos* mRNA localizing in the core, none were translating, whereas among the 89% of *suntag-nos* mRNA localizing in the outer phase and periphery, about half (52%) were translating (Fig. 2m). To confirm that this localization of scFv-GFP foci did not reflect reduced scFv-GFP availability in embryos, or its inability to reach the core of germ granules, we visualized *suntag-nos* translation using direct Suntag immunostaining with anti-GCN4 antibody. This approach revealed the same localization of translation mostly in the outer phase and periphery of germ granules (94.4 %) (Supplementary Fig. 3g, h). Furthermore, we designed a construct in which the 12 Suntag repeats were fused to MCP in order to recruit the MCP-Suntag fusion protein to germ granules using *nos-MS2* (*MS2* inserted into *nos* 3′UTR) (Supplementary Fig. 3i). When MCP-Suntag was visualized with scFv-GFP, we found a high colocalization (93%) with *nos-MS2* (Supplementary Fig. 3j, k). Importantly, co-staining of scFv-GFP with Osk to visualize germ granules showed that 31.7% of scFv-GFP foci localized to the core of the granules, demonstrating its capability to access the core (Supplementary Fig. 3l, m).

We conclude that mRNA translation is compartmentalized within germ granules, occurring in the outer phase and at the immediate periphery of the granules. In addition, mRNAs localized in the core of the granules are translationally repressed.

Translational repressors are not present within germ granules

The regionalization of *suntag-nos* mRNA translation within germ granules implied that translational regulators should be heterogeneously distributed within germ granules. We previously reported a role of Aub in *nos* mRNA translation activation through interaction with the translation initiation factors eIF3d and PABP that localized at the edge of germ granules[43]. Using STED imaging, we found that eIF3d and PABP accumulated in the outer phase and at the surface of germ granules, but not in the inner phase (Fig. 3a, b), and they colocalized with GFP-Aub using PCC(Costes) (Fig. 3j). We next investigated the localization of translational repressors known to regulate *nos* mRNA in early embryos. Whereas *nos* mRNA translation is activated in the germ plasm, it is repressed in the somatic part of early embryos through deadenylation by the CCR4-NOT deadenylation complex, and by a repressor complex containing Smaug, Cup, Trailer Hitch, and the RNA helicases Me31B -a DDX6 homolog- and Belle -a DDX3 homolog-[44]. We analyzed the localization of Smaug, Cup, Me31B and Belle in the germ plasm using STED microscopy and did not find colocalization of any of these proteins with the germ granule markers Osk or Aub using PCC(Costes) (Fig. 3c–e, g, j). In particular, these translational repressors never accumulated in the core of germ granules where mRNAs are not translated. However, we could observe Smaug, Cup, and Me31B foci at the surface of germ granules (Fig. 3c–e). Quantification of the distance between Smaug foci and germ granules (see "Methods"), revealed a significant localization of Smaug in germ granules and close proximity, with 28.3% of Smaug foci within 50 nm of germ granules (Fig. 3k). Smaug is known to interact with Osk in the germ plasm, preventing Smaug binding to *nos* mRNA and relieving translational repression[45,46]. Given Smaug foci localization at the surface of germ granules (Fig. 3c, k), this might be the site where the Smaug-Osk interaction takes place. Me31B was previously reported to be a component of germ granules[47]. Although Me31B was not found within germ granules in the germ plasm, it accumulated in the outer phase of germ granules at a later stage when germ granules enlarge by fusion in primordial germ cells (Fig. 3f), consistent with a recent study describing Me31B enrichment in germ granules at this stage[48]. We then addressed the relationships of the deadenylation machinery with germ granules by recording the localization of two subunits of the deadenylation complex, Not1, and CCR4, in the germ plasm. None of the subunits showed association with germ granules marked with Osk or Aub (Fig. 3h–j).

The lack of translational repressors inside germ granules suggests that mRNAs accumulating in the core of germ granules may be repressed due to their high mRNA compaction and/or partitioning of translational activators into the shell.

mRNA localization within the germ granule biphasic architecture depends on their translation status

Translation of the germ granule mRNAs, *nos*, *germ cell less* (*gcl*), *polar granule component* (*pgc*) and *Cyclin B* (*CycB*) is sequential[13]: *nos*
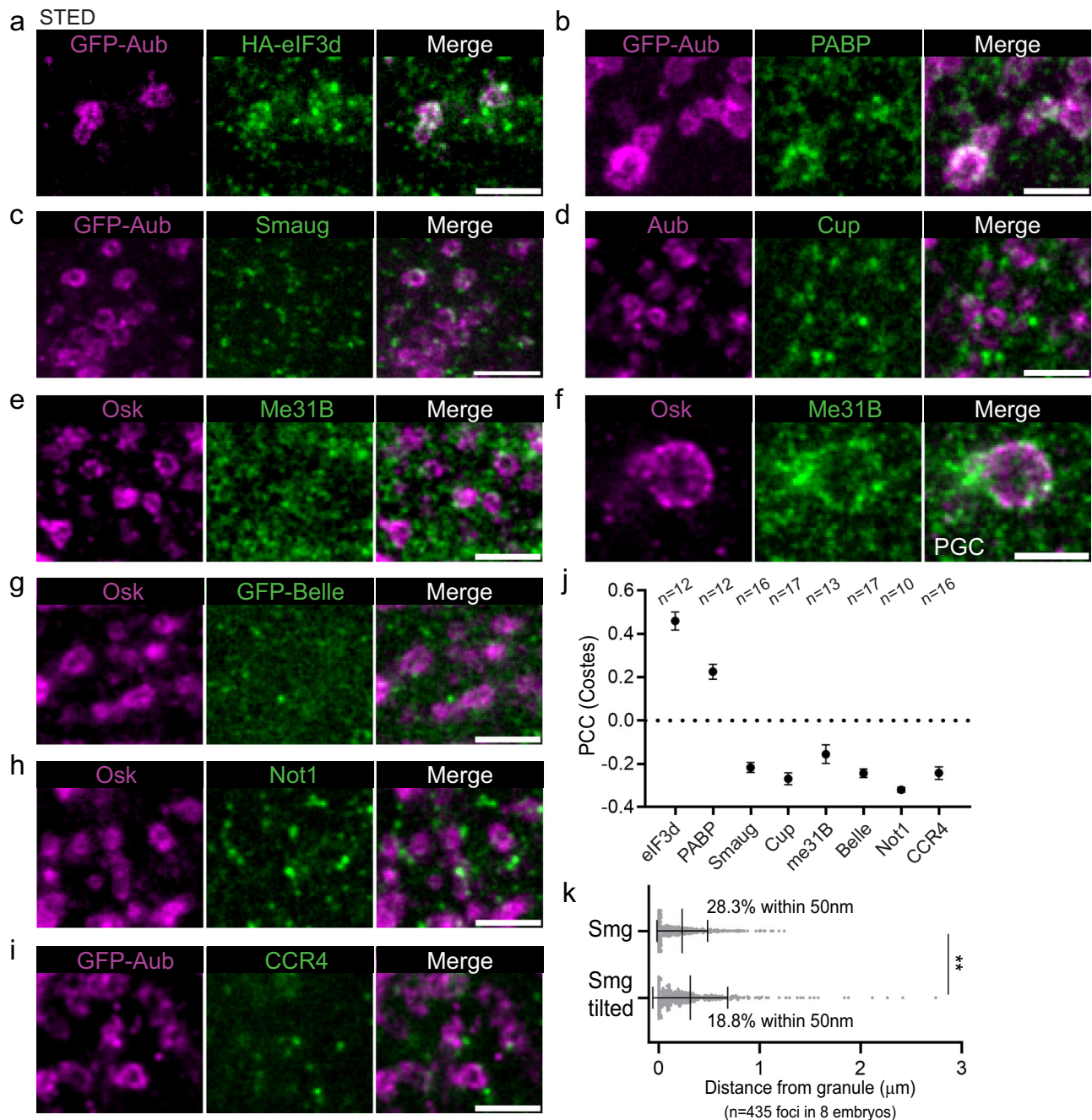
Fig. 3 | Localization of translation initiation factors and translational repressors in the germ plasm. a, **b** Localization of translation initiation factors. STED imaging of immunostaining of *UASp-GFP-Aub/UASp-HA-eIF3d; nos-Gal4/+* (**a**) and *UASp-GFP-Aub; nos-Gal4* (**b**) embryos with anti-GFP (magenta) to detect Aub, anti-HA (green) to detect eIF3d (**a**) and anti-PABP (green) (**b**). **c**–**i** Localization of translational repressors. STED imaging of immunostaining of *UASp-GFP-Aub; nos-Gal4, GFP-belle*, and wild-type embryos with antibodies to reveal the indicated proteins. Germ granule markers are in magenta and translational repressors are in green. A larger germ granule exemplifying those present at later stages in primordial germ cells (PGC) is shown in (**f**). **j** Quantification of colocalization of GFP-Aub or Osk with the indicated proteins using PCC(Costes) from images as in (**a**–**e** and **g**–**i**). Black circles represent the mean and error bars represent SEM. The number of embryos is indicated (*n*). **k** Quantification of the distance between Smaug (Smg) foci and the edge of germ granules marked with GFP-Aub from images as in (**c**). Vertical bars represent the mean and SD. **$p < 0.01$ using χ^2 test. $p = 0.0033$. Scale bars: 1 μm. Source data are provided as a Source Data file.

translation is already active at the onset of embryogenesis; *gcl* translation starts soon after, Gcl protein being visible 20–30 min after embryo deposition at 25 °C[13,49]; *pgc* translation takes place after primordial germ cell formation, 90 min after embryo deposition[13]; and *CycB* translation starts after primordial germ cell incorporation into the gonads, at 12–13 h of embryogenesis[50]. To understand how these mRNAs integrate within the biphasic organization of germ granules in relation with their translation status, we analyzed their localization

using immuno-smFISH with anti-Osk immunostaining to visualize germ granules, combined with STED microscopy. We found that *gcl*, *pgc*, and *CycB* mRNAs formed one to two foci within germ granules, consistent with their assembly in homotypic clusters[18,19] and that *nos* mRNA assembled in multiple foci, as previously reported[19], within and at the immediate periphery of germ granules (Fig. 4a–d). We used the number of nuclei to carefully stage embryos and classify them into early (≤2 nuclei, age 0–20 min) and late (>2 nuclei and before primordial
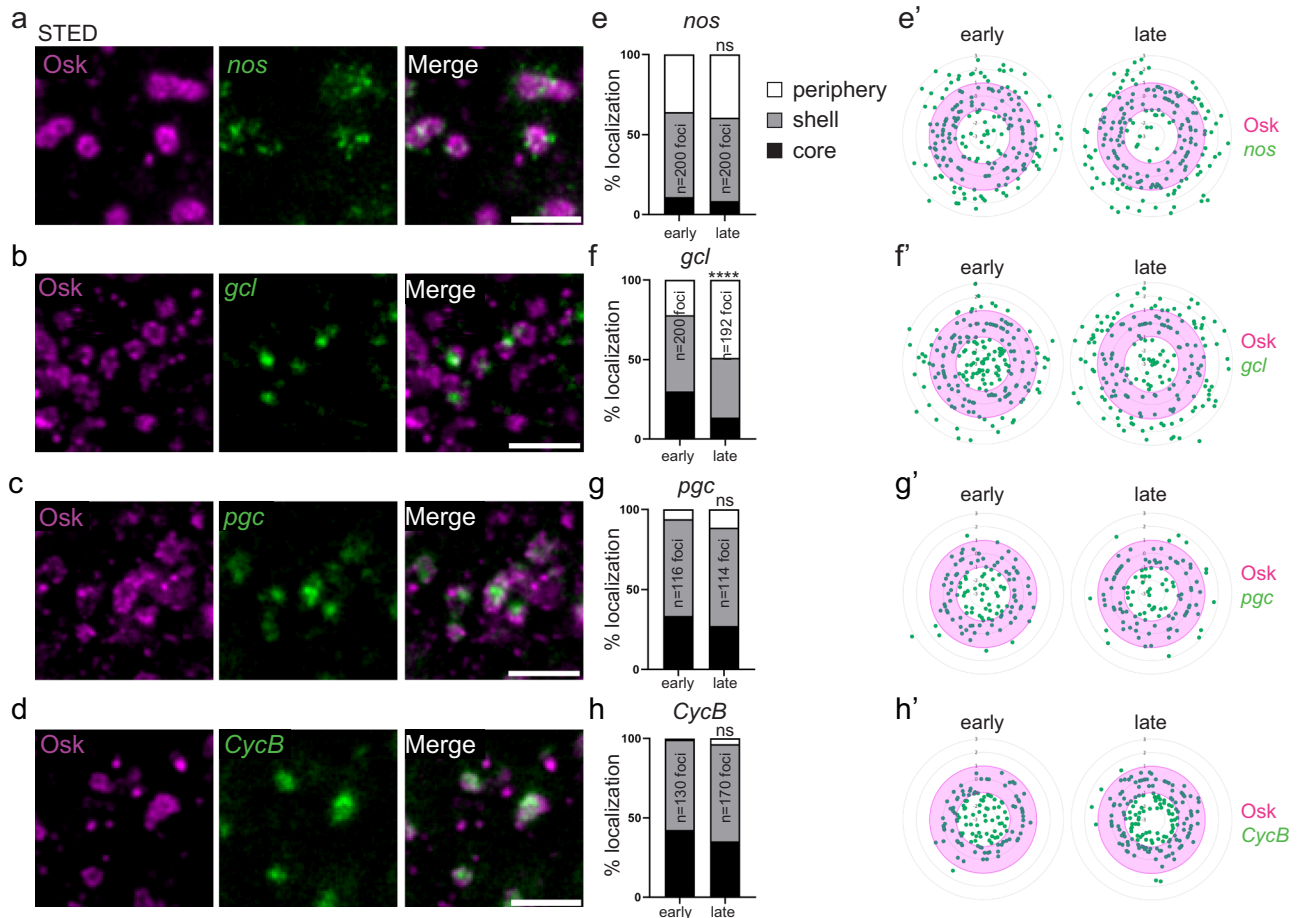
Fig. 4 | mRNA localization within germ granules. a–d STED images of immuno-smFISH of wild-type embryos (20–120 min) with anti-Osk (magenta) and smFISH probes (green) against *nos* (**a**), *gcl* (**b**), *pgc* (**c**), and *CycB* (**d**) mRNAs. **e–h** Percentage of localization of *nos*, *gcl*, *pgc*, and *CycB* mRNA foci in early (0–20 min) and late (20–90 min) wild-type embryos, in the core (black), in and at the surface of the shell (grey) and at the immediate periphery (white) of germ granules from images as in

(**a–d**). ns: non-significant, ****$p < 0.0001$ using the χ^2 test. $p = 0.61$ in (**e**), 1.49×10^{-18} in (**f**), 0.26 in (**g**) and 0.17 in (**h**). **e'–h'**, Radar plots of the relative localization of *nos*, *gcl*, *pgc*, and *CycB* mRNAs (green dots) within Osk immunostaining (magenta) in early (0–20 min) and late (20–90 min) embryos from images as in (**a–d**). The granule shell is in pink. Scale bars: 1 μm. Source data are provided as a Source Data file.

germ cell formation, age 20–90 min) stages. The localization of mRNA foci within germ granules was recorded in early and late-stage embryos. Each mRNA focus was categorized as localized in the core, the shell, or at the immediate periphery of germ granules. The localization of *nos* mRNA whose translation was active in both early and late stage embryos did not significantly change between both time points (Fig. 4e, e'). Similarly, the localization of *pgc* and *CycB* mRNAs whose translation started beyond the developmental period analyzed did not change between both stages (Fig. 4g–h'). In contrast, *gcl* mRNA localization changed after the onset of its translation (Fig. 4f, f'). While in early-stage embryos, 30% of *gcl* mRNA foci localized in the core of germ granules, this percentage decreased to 13.5% in late stage embryos. Therefore, upon translation, *gcl* mRNA relocalized from the core to the periphery of germ granules, showing that the distribution of mRNAs within germ granules correlated with their translation status.

To address mRNA orientation in relation with their translation within germ granules, we next designed smFISH probes directed against the 5′end and 3′end of *nos* (5′-*nos* and 3′-*nos*) as an example of translated mRNA, and *CycB* (5′-*CycB* and 3′-*CycB*) as an example of repressed mRNA (Supplementary Fig. 4a), and performed double smFISH or immuno-smFISH with anti-Osk antibody of embryos. Notably, *nos* mRNA 3′ends assembled in a single cluster per granule, surrounded by many smaller foci corresponding to *nos* 5′ends (Fig. 5a). The specificity of *nos* smFISH probes was confirmed by the lack of signal obtained with these probes in

nos[BN] mutant embryos (Supplementary Fig. 4b). In addition, we swapped the fluorophores between 5′-*nos* and 3′-*nos* probes and confirmed *nos* orientation with this new set of probes (Supplementary Fig. 4c). Using the new 3′-*nos* probe that provides a more defined signal, we could identify discrete central *nos* mRNA 3′ends (Supplementary Fig. 4c), and the same number of 5′-*nos* and 3′-*nos* foci per granule (Supplementary Fig. 4d). With regards to germ granule core/shell organization defined by Osk staining, *nos* 5′ends were predominantly localized in the shell and at the immediate periphery of germ granules, whereas *nos* 3′ends localized within the core and shell of germ granules (Fig. 5b–e). Interestingly, *CycB* mRNA showed the reverse orientation. *CycB* 5′ends were localized more internally than their 3′ends (Fig. 5f), and when compared to germ granule organization, *CycB* 5′ends localized within the core and shell of germ granules, whereas its 3′ends localized more externally in the shell and at the periphery of the granules (Fig. 5g-j).

Together, these results show mRNAs translocate from the core towards the shell and periphery of germ granules upon translation and that they have a specific orientation within the granules, 5′ends of translated mRNAs being localized externally.

Reducing translation increases mRNA compaction in germ granules

Egg activation that occurs upon egg laying triggers a massive remodeling of the maternal transcriptome landscape, involving drastic
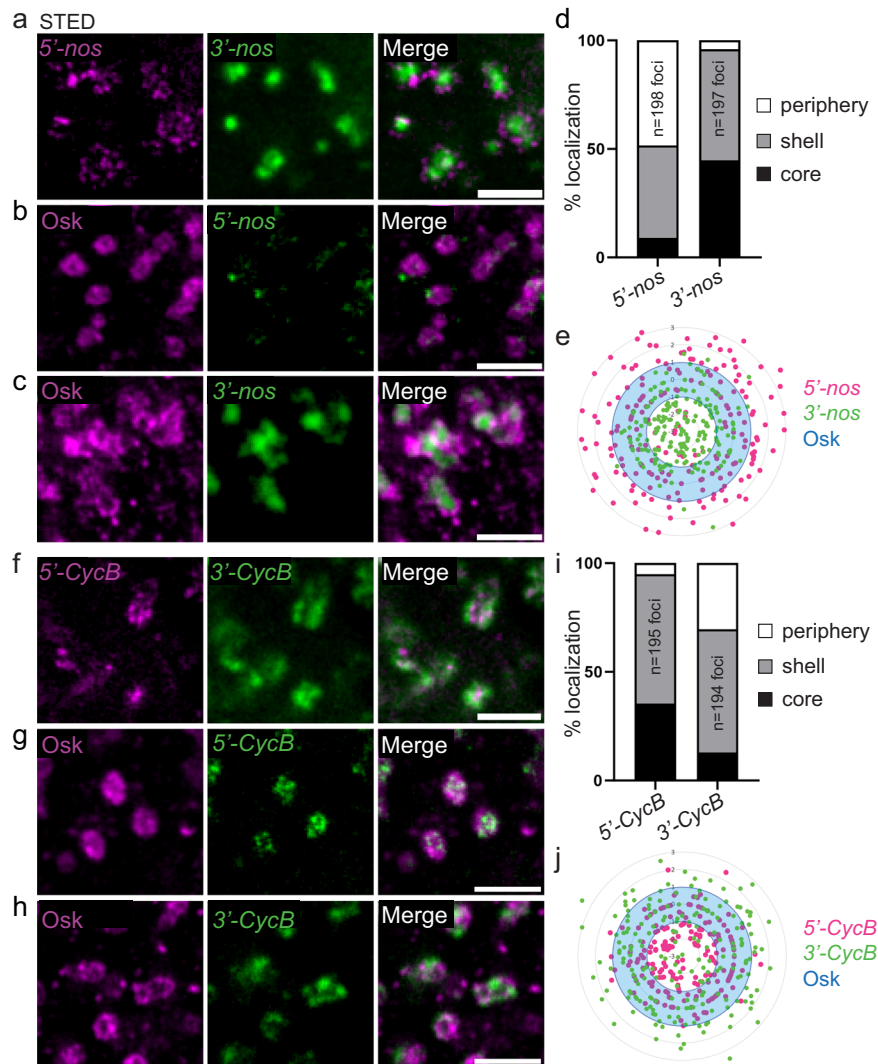
Fig. 5 | mRNA orientation within germ granules. a STED images of smFISH of wild-type embryos with *nos* 5'end (*5'-nos*, magenta) and 3'end (*3'-nos*, green) probes. **b, c** STED images of immuno-smFISH with anti-Osk antibody (magenta) as a marker of germ granules and *nos* 5'end (**b**) or 3'end (**c**) probes (green). **d** Percentage of *nos* 5'end and 3'end foci localized in the core (black), in and at the surface of the shell (grey), and at the immediate periphery (white) of germ granules from images as in (**b**, **c**). **e** Radar plot of the relative localization of *nos* 5'end (magenta dots) and 3'end (green dots) within Osk immunostaining (blue) in wild-type embryos from images as in (**b**, **c**). The granule shell is in blue. **f** STED images of smFISH of wild-type embryos with *CycB* 5'end (*5'-CycB*, magenta) and 3'end (*3'-CycB*, green) probes. **g, h**, STED images of immuno-smFISH with anti-Osk antibody (magenta) as a marker of germ granules and *CycB* 5'end (**g**) or 3'end (**h**) probes (green). **i** Percentage of *CycB* 5'end and 3'end foci localized in the core (black), in and at the surface of the shell (grey), and at the immediate periphery (white) of germ granules from images as in (**g**, **h**). **j** Radar plot of the relative localization of *CycB* 5'end (magenta dots) and 3'end (green dots) within Osk immunostaining (blue) in wild-type embryos from images as in (**g**, **h**). The granule shell is in blue. Scale bars: 1 μm. Source data are provided as a Source Data file.

changes in mRNA stability and translation efficiency[51,52]. The Pan gu (Png) kinase has a critical role in promoting translation at egg activation through the phosphorylation of several translational repressors[53]. We addressed whether *nos* mRNA translation at germ granules would be affected in *png* mutant embryos, making them an excellent genetic system to analyze the links between mRNA translation and localization within germ granules, if it was the case. Using immuno-smFISH and confocal imaging to visualize *suntag-nos* mRNA and scFv-GFP foci, we found a significant decrease in the number of *suntag-nos* mRNA clusters colocalizing with scFv-GFP, i.e., undergoing translation, in *png* mutant compared to control embryos (Supplementary Fig. 5a, b), whereas the number of *suntag-nos* mRNA molecules per cluster was not reduced (Supplementary Fig. 5c). Therefore, *suntag-nos* mRNA translation was reduced in *png* mutant embryos. We analyzed the distribution of *nos* and *gcl* mRNAs within germ granules in *png* mutant embryos using immuno-smFISH with anti-Osk antibody and STED imaging. Importantly, both *nos* and *gcl* mRNA localization were

affected in *png* mutant embryos where the percentage of mRNA foci localized in the core of germ granules increased at the expense of that at the periphery (Fig. 6a–d). In contrast, the localization within germ granules of *CycB* mRNA that was not translated at this stage, did not change in *png* mutant embryos (Supplementary Fig. 6a, b). Thus, decreasing translation led to a redistribution of translating mRNAs towards the inside of germ granules.

We next analyzed the orientation and conformation of *nos* mRNA within germ granules upon reduced translation using double smFISH with *nos* 5'end and 3'end specific probes and STED imaging. The 5'−3' orientation of *nos* mRNA within germ granules did not change in *png* mutant embryos, *nos* 5'end remaining localized externally to *nos* 3'end (Fig. 6e). However, both ends appeared closer to each other than in wild-type embryos. To measure the distance between *nos* 5'end and 3'end, we first determined the colocalization precision in our experimental conditions. We performed smFISH with the same *nos* probe labeled with two different fluorophores; we identified the centers of
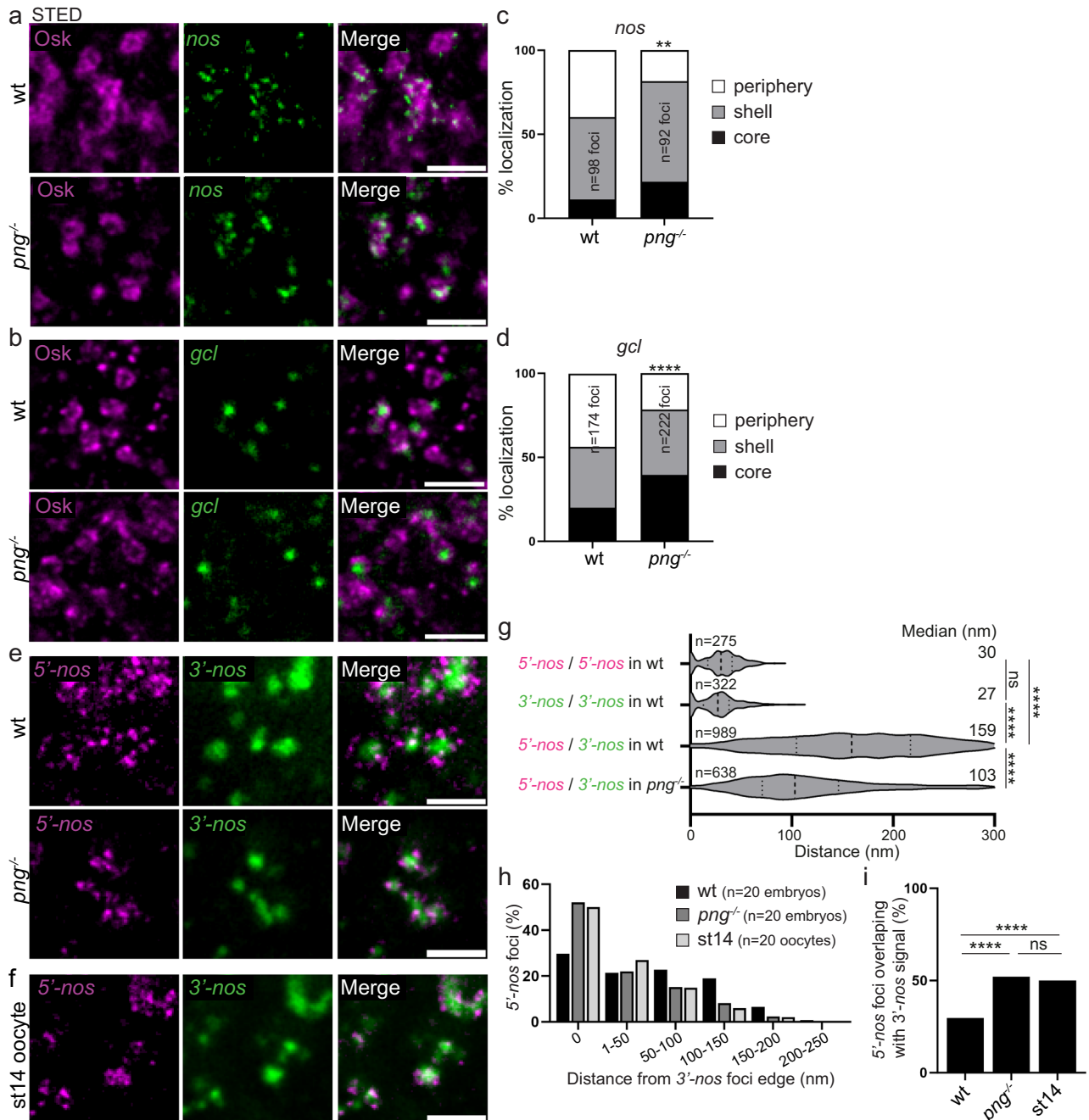
Fig. 6 | mRNA localization and compaction within germ granules depend on their translation. a, **b** STED imaging of immuno-smFISH of wild-type (top) and png^{1058} (bottom) embryos with anti-Osk antibody (magenta) as a marker of germ granule and smFISH probes (green) against *nos* (**a**) and *gcl* (**b**) mRNAs. **c**, **d** Percentage of localization of *nos* (**c**) and *gcl* (**d**) mRNA foci in wild-type and png^{1058} mutant embryos, in the core (black), in and at the surface of the shell (grey), and at the immediate periphery (white) of germ granules from images as in (**a**, **b**). **p < 0.01, ****p < 0.0001 using the χ^2 test. p = 0.0031 in (**c**) and 1.75×10^{-22} in (**d**). **e** STED images of smFISH against *nos* 5'end (*5'-nos*, magenta) and 3'end (*3'-nos*, green) in wild-type and png^{1058} mutant embryos. **f** STED images of smFISH against *nos* 5'end (*5'-nos*, magenta) and 3'end (*3'-nos*, green) in wild-type stage 14 oocytes. **g** Violin plots showing distance distribution of colocalizing foci (*5'-nos* to *5'-nos* and *3'-nos* to *3'-nos*) and 5'end to 3'end distances for *nos* mRNAs at germ granules in wild-type and png^{1058} mutant embryos, from STED images as in (**e**). Dashed lines inside the violin plots show first quartile, median, and third quartile. Median distances are indicated on the right. ns: non-significant, ****p < 0.0001 using unpaired two-tailed Student's t-test. p = 0.2 between *5'-nos/5'-nos* and *3'-nos/3'-nos*, p = 3.5×10^{-191} between *5'-nos/5'-nos* and *5'-nos/3'-nos* in wt, p = 1.3×10^{-218} between *3'-nos/3'-nos* and *5'-nos/3'-nos* in wt and p = 4.5×10^{-58} between *5'-nos/3'-nos* in wt and $png^{-/-}$. The number of measured distances is indicated (*n*). **h** Measurement of the distance between *nos* 5'end foci and the edge of *nos* 3'end foci in wild-type embryos, png^{1058} embryos, and wild-type stage 14 oocytes (st14), from images as in (**e**, **f**). The histogram shows the percentage of *nos* 5'end foci in each distance class. **i** Percentage of *nos* 5'end foci overlaps with *nos* 3'end foci in wild-type embryos, png^{1058} embryos and wild-type stage 14 oocytes (st14). ns: non-significant, ****p < 0.0001 using the χ^2 test. p = 2.64×10^{-129} between wt and $png^{-/-}$, p = 1.79×10^{-167} between wt embryos and stage 14 oocytes, and p = 0.15 between $png^{-/-}$ embryos and stage 14 oocytes. Scale bars: 1 µm. Source data are provided as a Source Data file.

each signal using a 2D Gaussian fitting and measured the distances between colocalizing signals (see "Methods")[54]. We recorded the median distances to be 30 nm and 27 nm for the 5′-nos and 3′-nos probes, respectively, indicating that we can resolve mRNA 5′end and 3′ end when they are distant by more than 30 nm (Fig. 6g). Using this approach, we found that the median distance between nos 5′end and 3′ end in wild-type germ granules was 159 nm, whereas it was reduced to 103 nm in png mutant embryos (Fig. 6g). We then recorded the range of distances between nos 5′end and 3′end by measuring the distance between the center nos 5′end signal and the edge of nos 3′end signal (see "Methods" and Supplementary Fig. 7) in wild-type and png mutant embryos. We observed that the proportion of nos 5′end overlapping with nos 3′end (distance = 0) increased in png mutant compared to wild-type embryos (Fig. 6h, i), at the expense of nos 5′end separated from nos 3′end by more than 50 nm. A similar increase in mRNA compaction was not observed with CycB mRNA in pgn mutant embryos (Supplementary Fig. 6c–e). Furthermore, the distance between 5′end and 3′end for CycB was closer than that for nos mRNA in wild-type embryos (compare Fig. 6h, i and Supplementary Fig. 6d, e).

In addition to png mutant embryos, we took advantage of another context where translation is reduced. A previous study based on GFP-Nos fusion protein reported that nos mRNA translation started at the posterior pole during oogenesis, in stage 13 oocytes[55]. However, using suntag-nos mRNA, we found that translation did not occur in stage 14 oocytes (Supplementary Fig. 8), suggesting that nos translation at germ granules was initiated or strongly increased following egg activation. We found that the distance between nos 5′end and 3′end was closer in stage 14 oocytes than in embryos, and similar to that in png mutant embryos (Fig. 6f–i).

These results strengthen the conclusion that mRNAs move towards the outer phase and periphery of germ granules when they are translated. They also reveal that mRNA conformation depends on their translational status, showing higher compaction when they are not translated and decompaction upon translation.

Translation is perturbed in a *tud* mutant that lost germ granule biphasic organization

We sought to perturb germ granule architecture in order to address its contribution to germ granule functions. We took advantage of a single point mutant of tud in the first Tudor domain, tud[A36] (Supplementary Fig. 9a), in which germ granules were described as rods instead of hollow spheres by electron microscopy[26]. Tud protein contains 11 Tudor domains. These domains are known to mediate interactions with other proteins, in particular through dimethylated arginines. Tudor domains in Tud have been proposed to serve as docking platforms for germ granule assembly[26], and indeed the multiple Tudor domains should generate multivalent interactions known to be instrumental in the formation of condensates by phase separation[56]. Aub undergoes symmetric arginine dimethylation and Tud recruits Aub to germ granules through interaction between several Tudor domains and Aub dimethylated arginines[57–60]. Interestingly, in tud[A36] mutant embryos, although germ granule mRNAs were shown to localize to the posterior pole, the formation of germ cells was strongly affected[26], suggesting a defect in mRNA translation at germ granules. Analysis of germ granules in tud[A36] embryos, using Osk immunostaining and STED imaging revealed a drastic alteration of germ granule organization. The biphasic structure was lost (Fig. 7a) and the size of germ granule was reduced to an average of 147 ± 28 nm instead of 279 ± 57 nm in wild-type embryos (Fig. 7b). Investigating suntag-nos translation in tud[A36] mutant embryos using immuno-smFISH and confocal imaging to record suntag-nos mRNA clusters and scFv-GFP foci, we found a strong decrease in translation (Fig. 7c). The percentage of translating suntag-nos mRNA clusters, i.e., colocalizing with scFv-GFP foci, decreased from 24.4% in wild-type embryos to 8.5% in tud[A36] mutant embryos (Fig. 7d), whereas suntag-nos mRNA localization to

germ granules was only slightly reduced (mean of 2.4 suntag-nos molecules per cluster in wild-type germ granules versus 2.1 in tud[A36]) (Supplementary Fig. 9b). We analyzed the localization of suntag-nos translation within germ granules using immunostaining to reveal scFv-GFP foci and Osk as a germ granule marker, visualized with STED microscopy. We confirmed a lower number of scFv-GFP foci in germ granules in tud[A36] embryos and these foci localized mostly at the periphery of germ granules or close to their surface (Fig. 7e, Supplementary Fig. 9c), indicating that the structure of tud[A36] germ granules was not compatible with translation inside the granules.

Aub activates nos mRNA translation initiation[43] and Vasa was also reported to play a role in activating translation[61]. We, therefore, asked whether Aub or Vasa recruitment to germ granules was impaired in tud[A36] embryos, which might contribute to reduced suntag-nos mRNA translation. Immunostaining to examine the posterior recruitment of Aub and Vasa together with Osk in tud[A36] mutant embryos showed that their recruitment was not affected as quantified using confocal imaging and measuring immunostaining intensity relative to that of Osk (Supplementary Fig. 9d–g). In addition colocalization of Aub with Osk analyzed using STED microscopy showed that Aub was recruited to germ granules in tud[A36] embryos, with a colocalization with Osk similar to that in wild-type embryos (Fig. 7f, g). Germ granule altered architecture in tud[A36] mutant might be the consequence rather than the cause of reduced translation levels. To address this question, we analyzed germ granule organization in tud[A36] stage 14 oocytes in which translation has not started yet or was occurring at very low levels. We found that the defects in germ granule architecture in stage 14 oocytes were similar to that recorded in tud[A36] embryos (Fig. 7h, i), indicating that altered granule organization preceded the burst of translation that took place at egg activation.

We conclude that translation is strongly reduced in tud[A36] mutant embryos due to the defective architecture of germ granules, although we cannot totally exclude the contribution of another Tud function. These results reveal tight links between germ granule core/shell organization and mRNA translation.

Discussion

In this manuscript, we use Drosophila germ granules as a model system to address the relationships between the multi-layered organization of biomolecular condensates and their functions. Drosophila germ granules ensure two opposite functions: storage of translationally repressed mRNAs and sequential translational activation of the same mRNAs. Using super-resolution STED microscopy, we find that these germ granules have a biphasic organization with an accumulation of protein components in their outer phase. Analyses of mRNA localization within germ granules combined with the suntag approach to record ongoing translation reveal that the storage of translationally repressed mRNAs takes place in the core of germ granules, whereas translation occurs in the shell and at the periphery of the granules. Therefore, the granule shell and periphery are permissive for translation, while the core is not. Using 5′end and 3′end probes of the same mRNAs, we show that mRNA orientation within germ granules reflects their translation status, 5′ends of translated mRNAs pointing towards the surface and periphery of germ granules. Moreover, mRNA compaction correlates with their translation levels, reduced translation leading to higher mRNA compaction, as it was described recently in stress granules[54]. Finally, taking advantage of a mutant in which the biphasic architecture of germ granules is lost, we show that translation is linked to their core/shell organization. These results demonstrate the functional compartmentalization of germ granules, a process that is central for germ cell specification and development.

We propose a model in which repressed mRNAs are stored in a compacted state in the core of germ granules and translocate to the outer phase for translation (Fig. 7j). To our surprise, we did not identify translational repressors accumulating in the core of germ granules.
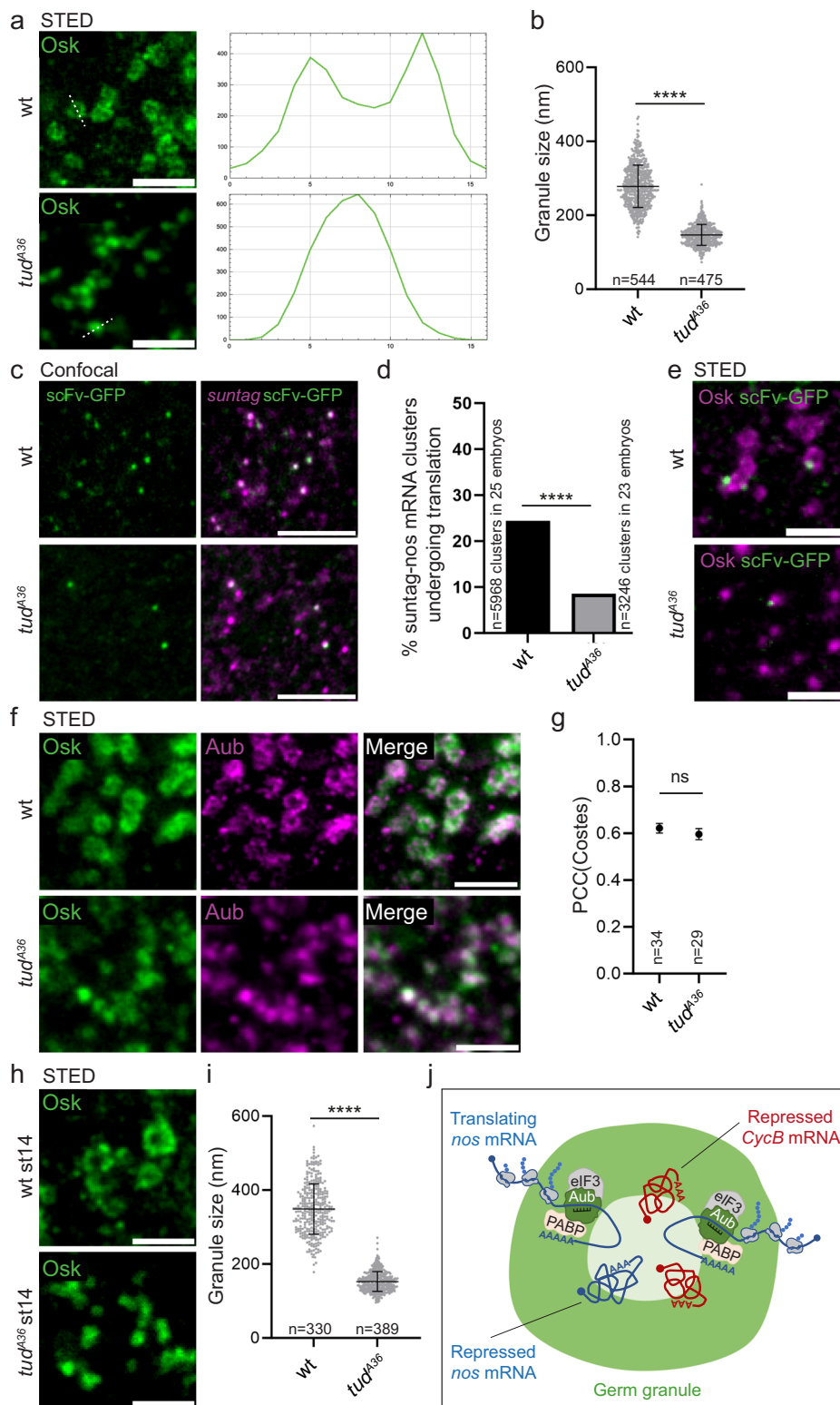
Together with the information that untranslated mRNAs have their 5′-and 3′regions closer than translated mRNAs, and are thus more compacted, these data suggest that the lack of translation in the core of germ granules would involve a mechanism based on mRNA compaction and compartmentalization away from the translation machinery, independent of specific translational repressors. Nonetheless, several lines of evidence point to a second mechanism involving translational repressors. First, the 3′end of the repressed mRNA, *CycB* is oriented towards the shell and periphery of germ granules, and we also

find the association of Smaug translational repressor with the surface and periphery of the granules, suggesting that Smaug might bind repressed mRNA 3′UTRs in this location. Smaug interaction with Osk in this external part of germ granules would relieve translational repression[45,46]. Second, *suntag-nos* translation at germ granules is reduced in *png* mutant embryos and Png kinase is known to relieve translational repression through phosphorylation of translational repressors[53]. These data suggest the implication of translational repressors in translational regulation at germ granules. Third,

Fig. 7 | nos mRNA translation depends on germ granule biphasic architecture. **a** STED images of wild-type and *tud^{A36}/Df(2 R)Pu^{rP133}* (*tud^{A36}*) embryos immunostained with anti-Osk antibody. Fluorescence intensity was recorded along the white dotted line (right). **b** Measurement of germ granule size in wild-type and *tud^{A36}/Df(2 R)Pu^{rP133}* (*tud^{A36}*) embryos from images as in (**a**). Horizontal bars represent the mean and SD. ****$p < 0.0001$ using unpaired two-tailed Student's t-test. $p = 2.4 \times 10^{-248}$. **c** Immuno-smFISH of *nos-suntag-nos/+; nos-scFv-GFP/+* (wild-type) and *nos-suntag-nos tud^{A36}/Df(2R)Pu^{rP133}; nos-scFv-GFP/+* (*tud^{A36}*) embryos with anti-GFP nanobody (green) to reveal scFv-GFP and *suntag* smFISH probe (magenta). **d** Percentage of *suntag-nos* mRNA clusters colocalizing with scFv-GFP foci, i.e., undergoing translation, in *nos-suntag-nos/+; nos-scFv-GFP/+* (wild-type) and *nos-suntag-nos tud^{A36}/Df(2R)Pu^{rP133}; nos-scFv-GFP/+* (*tud^{A36}*) embryos from images as in (**c**). ****$p < 0.0001$ using χ^2 test. $p = 2 \times 10^{-77}$. **e** STED images of immunostaining of *nos-suntag-nos/+; nos-scFv-GFP/+* (wild-type) and *nos-suntag-nos tud^{A36}/Df(2 R) Pu^{rP133}; nos-scFv-GFP/+* (*tud^{A36}*) embryos with anti-Osk antibody (magenta) and anti-GFP nanobody (green) to reveal scFv-GFP. **f** STED images of immunostaining of wild-type and *tud^{A36}/Df(2 R)Pu^{rP133}* (*tud^{A36}*) embryos with anti-Osk (green) and anti-Aub (magenta) antibodies. **g** Quantification of colocalization between Osk and Aub using PCC(Costes). Black circles represent the mean and error bars represent SEM. The number of embryos is indicated (*n*). ns: non-significant using unpaired two-tailed Student's t-test. $p = 0.42$. **h** STED images of immunostaining of wild-type and *tud^{A36}/Df(2 R)Pu^{rP133}* (*tud^{A36}*) stage 14 oocytes with anti-Osk antibody. **i** Measurement of germ granule size in wild-type and *tud^{A36}/Df(2 R)Pu^{rP133}* (*tud^{A36}*) stage 14 oocytes from images as in (**h**). Horizontal bars represent the mean and SD. ****$p < 0.0001$ using unpaired two-tailed Student's t-test. $p = 6.2 \times 10^{-209}$. **j** Model of functional compartmentalization of germ granules. The scheme represents a biphasic germ granule with main protein components accumulating in the outer phase (green). Repressed mRNAs in a condensed state accumulate towards the granule core. Translation takes place in the outer phase and at the periphery of the granule. Translational activators (eIF3 and PABP) are found in the outer phase. Translated mRNAs are less condensed and anchored to the granule core from their 3′region, whereas their 5′end is oriented toward the outer phase and periphery of the granule. mRNAs translocate from the core to the outer phase during translation. Scale bars: 1 μm. Source data are provided as a Source Data file.

consistent with this, translational activation of germ granule mRNAs is sequential, again suggesting the role of specific repressors, or combinations of repressors whose effect would be relieved sequentially to achieve timely translation of specific mRNAs.

A major information from this study is that *Drosophila* germ granules have a function in translation. These granules are not incidental condensates regarding the translation of germ granule mRNAs[4] as translation of these mRNAs does not take place anywhere else in the embryo. Therefore, germ granules have an essential function in localized translation of specific mRNAs, which is required for germ cell development. Another key finding is the fact that translation takes place in a defined region of germ granules, the outer phase, indicating that the biophysical properties of this outer phase allow translation. Quantifications of *nos* mRNA levels in germ granules have shown that these levels do not decrease with time, up to the formation of primordial germ cells[62]. This indicates that *nos* mRNAs might be translated several times at germ granules without decay. These consecutive rounds of translation would be possible due to the capacity of the outer phase to allow translation, bypassing the necessity for mRNAs to leave germ granules to be translated, as it is the case in *C. elegans*[22,23]. Indeed, we found that translation initiation factors concentrate in this phase of germ granules. Thus, in addition to a role in localizing translation within the embryo, germ granules might be involved in increasing translation efficiency through the outer phase properties that would allow consecutive rounds of mRNA translation in the absence of decay.

RNA granules have a recognized role in mRNA storage (e.g., P bodies and stress granules), but their function in translational activation has remained more elusive and is currently an emerging question. A recent study showed that translation can occur in stress granules, although these granules are mostly composed of untranslated mRNAs[63]. In addition, translating mRNAs were also found capable of transiently docking to the surface of stress granules[64]. More recently, another study revealed that the formation of RNA granules driven by the FXR1 protein led to the translation of mRNA targets through translation initiation factor recruitment, thus identifying the first RNA condensate specialized in translation activation[65]. A recent analysis of zebrafish embryo germ granules reported that mRNA translation required their translocation to the granule periphery[66]. Finally, while this manuscript was under review, another study reporting translation at the surface of *Drosophila* germ granules was published[67]. These data align with previous electron microscopy analyses showing polysomes emerging from the surface of germ granules[25]. Here, we found that translation occurs in a specific phase of germ granules, the outer phase, highlighting the functional relevance of RNA granule higher-order organization. Whether such a functional organization is a conserved feature of germ granules remains an open question. In favor of this possibility, it was shown that during mouse spermatogenesis, translational activation coincided with the recruitment of eIF3f by Miwi (the mouse homolog of Aub) to the edge of the chromatoid body[68]. Understanding how translation is linked to the formation and biophysical properties of a specific phase of germ granules represents an interesting challenge for future studies.

Methods

Drosophila lines
w^{1118} was used as wild-type (wt). Mutant alleles and transgenic lines were: *UASp-GFP-Aub*[69], *nos-Gal4-VP16*[70], *UASp-HA-eIF3d*[43], *UASp-osk-bcd3′UTR* (short *osk*)[71], *Vasa-GFP^{KI}*, *GFP-Tud^{KI}* and *vasa-tdTom^{KI72}*, *nos-scFv-GFP*[40], *yw nos-MS2-5 nos-MS2-25*[73], *nos^{BN}/TM3sb*[74], *bel^{CC00869}*[44,75], *png^{1058}/FM6a*[76] and *tud^{A36}/Cyo*[26], *Df(2 R)Pu^{rP133}/CyO*. The *nos-suntag-nos* and *nos-MCP-suntag* lines were generated in this study by PhiC31 recombination into the *attP40* and *attP9A* sites, respectively. To record translation, females from the *nos-scFv-GFP* line were crossed with males of the *nos-suntag-nos* line. The genotypes of embryos (aged 0–2 h or less) indicated throughout were the genotypes of mothers. Females of the indicated genotypes were crossed with wt males.

Cloning and recombineering
To produce the *nos-suntag-nos* transgene, the sequence coding for 12 Suntag repeats was amplified by PCR from a clone provided by Bertrand[34]. The PCR fragment was cloned after the *nos* start codon into the pBSKS-R5561 plasmid that contains a 5.7 kb *nos* genomic fragment (a gift from Wharton[77]), using NEBuilder HiFi DNA Assembly (NEB). The *nos* genomic fragment containing *suntag* sequence was digested by *EcoR*I and *Not*I and cloned into the *pattB* vector (DGRC #1420) digested by *EcoR*I and *Not*I. The resulting plasmid was validated by sequencing and sent for injection (BestGene Inc) to be inserted into the *Drosophila* genome by PhiC31 recombination at the *attP40* site. To produce the *nos-MCP-suntag* transgene the sequence coding for 12 Suntag repeats was amplified by PCR. The PCR fragment was cloned using NEBuilder HiFi DNA Assembly (NEB) in frame with MCP coding sequence into the *pNosPE_MCP-TagRFPT-NLS* plasmid that contains a *nos* promoter, *nos* 5′ *UTR*, MCP coding sequence in frame with RFPt coding sequence (a gift from Dufourt[40]) digested by *HindIII* and *BamHI* to remove the RFPt sequence. The resulting plasmid was validated by sequencing and sent for injection (BestGene Inc) to be inserted into the *Drosophila* genome by PhiC31 recombination at the *attP9A* site.

Immunostaining
0–2 h-embryos were collected in a basket from plates, washed in tap water and dechorionated using commercial bleach for 2 min, and rinsed. Embryos were then fixed at the interface of a 1:1 solution of formaldehyde 36%/heptane for 5 min, followed by 100% methanol

devitellinization. Embryos were progressively rehydrated in 75%, 50%, and 25% methanol diluted in PBS 0.1% Tween, blocked in 1% BSA for 1 h for confocal imaging or 10% BSA for 3 h for STED imaging, and incubated overnight with primary antibodies. Secondary antibody incubation, after washes in PBS 0.1% Tween, was performed for 1 h at room temperature. Embryos were mounted in Vectashield (Vector Laboratories) for confocal imaging or Abberior liquid anti-fade (Abberior) for super-resolution imaging (STED, OMX and Airyscan). For super-resolution imaging the posterior pole of embryos was sliced using a thin needle in mounting medium and mounted posterior side up (Supplementary Fig. 1a). For stage 14 oocytes, ovaries were dissected from well fed females in Schneider medium and fixed in a chelating solution (1:1 heptane/PBS 1X, 50 mM EGTA pH8, 10.24% formaldehyde) to prevent egg activation, for 1.5 h at room temperature. Then ovaries were rinsed three times in PBS 0.1% Tween, transferred to a dissection dish where oocytes were dissociated from the rest of the ovary by multiple pipetting. Oocytes were put on a frosted slide and rolled with another frosted slide to remove chorion and vitelline membrane. Oocytes were transferred in a tube and processed for immunostaining as described for early embryos. Primary antibodies used were: mouse anti-Aub (1/1000, clone 4D10, a gift from M. Siomi,[78]), rabbit anti-CCR4 (1/200)[79], rabbit anti-Cup (1/1000, a gift from R. Wharton,[80]), rabbit anti-Me31B (1/2000, a gift from A. Nakamura,[81]), rabbit anti-Nos (1/1000, a gift from A. Nakamura), mouse anti-Not1 (1/100, clone 2G5,[79]), rabbit anti-Osk (1/1000, this study), rabbit anti-PABP (1/500, a gift from A. Vincent), rabbit anti-Smg (1/1000,[82]), rabbit anti-Tud (1/500, a gift from P. Lasko,[83]), mouse anti-HA (1/2000, ascites produced from clone 12CA5), rat anti-Vasa (1/50, Developmental Studies Hybridoma Bank), rabbit anti-GFP (1/1000, Invitrogen), mouse anti-GCN4 (1/1000, clone C11L34, Bio-Techne) and mouse anti-GFP (1/1000, Roche). Secondary antibodies used were: FluoTag®-X4 anti-GFP nanobodies StarRed or Atto488 (1/500, NanoTag Biotechnologies), goat anti-rabbit IgG Alexa-488 (1/800, Invitrogen), donkey anti-rabbit IgG Cy5 (1/1000, Jackson ImmunoResearch), goat anti-mouse IgG StarRed (1/1000, Abberior), goat anti-rabbit IgG StarRed (1/1000, Abberior), and goat anti-rabbit IgG Star580 (1/1000, Abberior).

smFISH and Immuno-smFISH

smFISH on 0–2 h-embryos were performed as previously described[43] with smFISH probes from Stellaris. For immuno-smFISH, rehydrated embryos were post-fixed in 4% formaldehyde for 20 min, rinsed three times for 10 min in PBS 0.1% Tween, and processed for smFISH followed by immunostaining. smFISH on stage 14 oocytes were performed as previously described[84] using 10% formamide. Probe sequences for *nos*, *gcl*, *pgc*, and *CycB* are listed in ref. [18]; the *MS2* probe is described in ref. [85]. Probe sequences to detect *suntag*, *nos* 5'end, *nos* 3'end, *CycB* 5'end and *CycB* 3'end are listed in Supplementary Tables 1–5. Probes were coupled to Cal Fluor 590 (*nos*, *gcl*, *pgc*, *CycB*, *suntag*, 5'-nos, 3'-nos, 3'-CycB, and *MS2*) or Quasar 670 (*nos*, 5'-nos, 3'-nos, and 5'-CycB).

Puromycin treatment

To treat embryos with puromycin, we adapted the permeabilization protocol previously described[86]. Dechorionized embryos were put in a 1:1 solution of DL-limonene (Sigma)/heptane with a 100 μl drop of PBS 1X containing 2 mg/ml puromycin (Sigma). Puromycin was initially diluted in water at 50 mg/ml. For control embryos, the puromycin solution was replaced by water alone. Embryos were shaken at maximum speed on a rotating plate for 40 min, rinsed in heptane, and processed for immunostaining.

Generation of anti-Osk antibody

The open reading frame of *osk* (short isoform) without the start codon was cloned after the *GST* sequence into the *pGEX-4T-1* vector to express a GST-Osk fusion protein in BL21 *E. coli* bacteria. The GST-Osk fusion protein was isolated on an acrylamide gel, purified using columns (Amicon), and injected into rabbits by Agro-Bio. The polyclonal rabbit antibody against this fusion protein was validated using immunostaining in ovaries and embryos.

Fluorescence microscopy

Confocal microscopy was performed using a Leica SP8 confocal scanning microscope with objectives 20X Plan Apochromat 0.75 NA Imm Corr for whole embryos (Supplementary Fig. 2a, b and 3b) or 63X Plan Apochromat 1.4 NA oil DIC for other confocal images. STED microscopy was performed using an Abberior STED super-resolution microscope controlled by Imspector software (Abberior Instruments) using a 100X Plan SuperApochromat 1.4 Oil objective. Excitation and depletion laser powers were adjusted according to the strength of the signal to optimize the resolution without bleaching the sample as follows. Excitation laser powers were set to collect, in confocal mode, approximately 200 grey levels for granule staining and 100 grey levels for other stainings. The optimal STED laser power was defined as the value giving the best resolution, and at the point where resolution was not improved while signal-to-noise ratio was decreasing. Resolution scales with the square root of the applied intensity and increasing laser power results in a marginal benefit in resolution when the optimal resolution is reached[87]. Pixel size was set to 30 nm. Resolution in our imaging conditions was 60 ± 12 nm, assessed by measuring the full width at half maximum of the PSF (Point Spread Function) of the smallest structure imaged in our samples (*5'-nos* signal in the soma). No pixel shift correction was applied as red and far-red signals were obtained from the same depletion laser aligned on the excitation lasers and photons collected followed the same optic path before spectral detection. In addition, SuperApochromat objective corrects the chromatic and spherical aberrations. Laser alignments were checked monthly and alignment measurements on tretraspeck 100 nm beads showed a shift of less than half a pixel. For OMX microscopy, 3D-SIM acquisitions were performed on a Deltavision OMX V4 and reconstructed using SoftWoRx software. The OMX used was equipped with a 100X Plan Apochromat NA1.4 Oil PSF graded objective and EMCCD cameras. For two color imaging in OMX, both channels were acquired sequentially but in immediate temporal proximity to minimize drift and crosstalk. In addition, multiple channels were realigned following manufacturer's procedures and calibration using the provided target slide. OMX image quality was assessed using SIMcheck, a FIJI plugin that assesses SIM reconstructed image quality through metric evaluation on the raw images, as previously described[88]. All images conformed to the requirements for intensity profile, modulation contrast to noise ratio and minimum to maximum intensity ratio. Airyscan microscopy was performed using confocal Zeiss LSM980 AiryScan II 8Y run by Zeiss Zen Blue software using a 63X Plan Apo oil 1.4NA objective.

Transmission electron microscopy (TEM)

For TEM, 0–1 h-embryos were collected in a basket from plates, washed in tap water and dechorionated using commercial bleach for 2 min and rinsed. Embryos were then fixed in heptane saturated with 12.5% glutaraldehyde in PHEM buffer (60 mM PIPES, 25 mM HEPES, 10 mM EGTA, 4 mM $MgSO_4 \cdot 7 H_2O$; EM grade) for 20 min at room temperature. The vitelline membrane was manually removed and the posterior poles were dissected and fixed in 2.5% glutaraldehyde in PHEM buffer overnight at 4 °C. Embryo posterior poles were post-fixed in 0.5% osmic acid + 0.8% potassium Hexacyanoferrate trihydrate for 2 h at dark and room temperature. After two washes in PHEM buffer, they were dehydrated in a graded series of ethanol solutions (30–100%). The embryo posteriors were embedded in EmBed 812 using an Automated Microwave Tissue Processor for Electronic Microscopy (Leica EM AMW). Ultra-thin sections of 70 nm were cut (Leica-Reichert Ultracut E), mounted on formvar-coated slotted

copper grids, and counterstained with uranyl acetate 1.5% in 70% ethanol and lead citrate. Stained grids were observed using a Tecnai F20 transmission electron microscope at 120KV, at the Electronic Microscopy facilities (Institut des Neurosciences de Montpellier).

Image analyses and quantifications

Before image analysis, all images were filtered with a Gaussian blur to reduce the noise and smooth the image. All images presented in the figures were filtered with Gaussian blur. No deconvolution was applied.

Quantification of mRNA molecule numbers. mRNA content in germ granules was quantified using FISH-quant[34,41]. Briefly, the mean intensity of single mRNA molecule was calculated from the signal of single particles in the soma as they mostly correspond to single mRNA molecules (83% of single particles for *nos* mRNA[42]). To determine the number of mRNA molecules present in each mRNA cluster at the posterior pole, the integrated intensity of each cluster was divided by the integrated intensity of the mean single mRNA molecules.

Quantification of germ granule size and shell size. On STED acquisitions of Osk or Aub immunostaining, we applied a Laplacian Gaussian filter to better define the signal edges. A line was drawn through the diameter of each granule and intensities along the line were measured using FIJI plot profile, giving two peaks that reflected the donut-like shape of germ granules (Fig. 1a). To determine the limit of the signal, we measured the full width at half maximum of the PSF for each peak and between the most external part of each peak, allowing the measurement of the granule diameters and shell thickness. From this, we defined the core and shell of germ granules. The surface of germ granules corresponded to their external edge, and the periphery corresponded to the cytoplasm surrounding the granule up to 200 nm. This value was chosen as we never observed RNAs or scFv-GFP foci with distances from the granule surface larger than this.

Quantification of the localization of mRNAs or scFv-GFP foci within the germ granule biphasic structure. To analyze the localization of mRNA foci (visualized either with the full-length, the 5′end, or the 3′end probes) or scFv-GFP foci within germ granule biphasic organization, we first applied a Laplacian Gaussian filter on the channel showing the germ granule staining to define the signal edges and thus the compartments (core, shell, periphery). Then mRNA coordinates were determined using RS-FISH ImageJ plugin[89]. A line was drawn across the granule and mRNA foci and pixel intensities along the line were recorded on Fiji Plot profile. The distance between the peak of the shell and the peak of the mRNA focus was measured on the plot. If the mRNA focus was located toward the external part of the granule, the measure was given a positive value. If the mRNA focus was toward the internal part of the granule, it was given a negative value. As the size of the shell is not identical between granules, the shell size was also measured for each measurement of the distance between the shell peak and mRNA focus, allowing us to determine the position of the mRNA focus within the granule using the following ratio:

distance between the peak of mRNA focus and the peak of the shell / (shell size/2).

If the ratio was > 1, the RNA focus was classified as "periphery". If the ratio was ≤ −1, the RNA focus was classified as "core". If the ratio was > −1 and ≤ 1, the RNA focus was classified as "shell". Quantifications of these ratios were shown as graphs, and the localization of mRNA foci were represented on hypothetic granules using radar plots. The same method was applied to quantify the position of scFv-GFP foci within germ granules.

Analysis and quantification of colocalization of scFv-GFP foci with suntag mRNA clusters and/or germ granules. On confocal images, germ granules appear as full dots or foci. To measure the association of scFv-GFP foci with germ granules or *suntag* mRNA clusters, we used FIJI plugin ComDet v.0.5.5 (https://github.com/UU-cellbiology/ComDet) to define the different foci and measure their colocalization. To visualize the colocalization of scFv-GFP foci with *suntag* mRNA clusters at germ granules (i.e., translation at germ granules, Supplementary Fig. 3c), we segmented the signals from *suntag* smFISH and scFv-GFP and created a mask that showed their colocalization (translation foci) using FIJI Image Calculator function. We then overlaid this mask on the channel showing germ granules visualized with anti-Osk immunostaining and quantified the colocalization of translation foci with germ granules.

Colocalization precision. To determine the colocalization precision of smFISH probes under our imaging conditions, distances between signals obtained with the same probe labeled with two different fluorophores were measured. Embryos were hybridized with a mix of oligos labeled with Quasar 670 and the same oligos labeled with Cal Fluor Red 590. This was performed for the *5′-nos* and *3′-nos* probes. The center of each signal was determined by 2D Gaussian fitting using RS-FISH plugin[89], and the distance between the signal centers from the two channels was measured using a FIJI plugin developed previously[90]. For measurements of *5′-nos* to *3′-nos* distances in wild-type and *png* mutant embryos, 300 nm was chosen as cutoff to avoid assigning signals from neighboring granules. This value was chosen from observations that 5′end to 3′end distances rarely extended beyond this cutoff and those that did corresponded to wrongful assignments.

Distance and colocalization between mRNA 5′end and 3′end. To measure the distance between *nos* mRNA 5′end and 3′end probes, the 3′end signal was segmented and defined as ROI. 5′end foci were identified using FIJI plugin ComDet v.0.5.5 (https://github.com/UU-cellbiology/ComDet) and their center was mapped by multipoint selection and added as ROI. The minimal distance between the edge of the 3′end ROI and the center of the 5′end foci was calculated using a FIJI plugin developed previously[90]. Overlap corresponds to a distance of 0.

Distance between Smaug foci and germ granules. To analyze the distance between Smaug foci and germ granules, Smaug signals above threshold were identified using the Fiji Find Maxima function. The signal for the granule corresponding to anti-Osk immunostaining was segmented and defined as ROI. The minimal distance between the edge of the granule ROI and the center of Smaug foci was calculated using a FIJI plugin developed previously[90]. As a control (Smg tilted), Smaug channel was horizontally and vertically rotated and the same measurement was performed.

Protein colocalization within germ granules. For images acquired with STED imaging, the degree of colocalization between signals corresponding to two immunostaining was quantified using PCC(Costes). The PCC method determines a threshold based on the mean fluorescence intensity for each signal. Then, the method analyzes each pixel and evaluates if signals are above or below their respective threshold, increasing PCC value if both signals go to the same direction, decreasing its value if they go to opposite directions. PCC ranges from 1 that indicates perfect colocalization, to −1 that indicates exclusion. To validate the significance of this colocalization, the PCC(Costes) value was calculated for each image. Briefly, images were randomized by shuffling pixels, the PCC value was calculated and compared to the original image. This process was repeated 200 times to evaluate the significance of the original picture. Costes *p*-value ranges from 0 to 1, where 0 indicates random colocalization and 1 indicates significant colocalization.

Quantification of germ granule main component levels. To quantify the level of Aub and Vasa in *tud*[436] mutants, ROIs delimiting the germ

plasm on maximum Z projection of 40 planes from confocal images were defined. The fluorescence-integrated density of Aub or Vasa was measured and normalized to Osk fluorescence-integrated density levels.

Statistics and reproducibility

Statistical tests were performed using GraphPad. For each figure, the tests are indicated in the figure legend. Each experiment was repeated two to thirteen times (see detail below); quantifications were at least from two independent replicates. No statistical method was used to predetermine sample size. No data were excluded from the analyses. The Investigators were not blinded to allocation during experiments and outcome assessment. Randomization was used in Figs. 3j, 7g and Supplementary Fig. 1d, and performed as explained above in the *Image analyses and quantifications* section. The number of times that experiments were repeated with similar results are as follows. Figure 1a: 2, 5, 3 and 4; Fig. 1b, c: 2; Fig. 2b, e: 13; Fig. 2d: 4; Fig. 2j: 5; Fig. 3a, d, e, f, h: 2; Fig. 3b, c, g, i: 3; Fig. 4a, b: 3; Fig. 4c, d: 2; Fig. 5a: 13; Fig. 5b: 6; Fig. 5c, f: 5; Fig. 5g, h: 3; Fig. 6a: 6; Fig. 6b: 4; Fig. 6e: 2; Fig. 6f: 4; Fig. 7a, f: 3; Fig. 7c: 6; Fig. 7e: 2; Fig. 7h: 3 and 4; Supplementary Fig. 1b: 4; Supplementary Fig. 1c, e, f: 2; Supplementary Fig. 2a, b: 3; Supplementary Fig. 2d: 2; Supplementary Fig. 3b, e, f, g, j: 2; Supplementary Fig. 3c, l: 4; Supplementary Fig. 4b: 2; Supplementary Fig. 4c, d: 3; Supplementary Fig. 5a: 2; Supplementary Fig. 6a, b: 2; Supplementary Fig. 8: 3; Supplementary Fig. 9d, f: 2.

Reporting summary

Further information on research design is available in the Nature Portfolio Reporting Summary linked to this article.

Data availability

All data are available in the main text or Supplementary Information. Source data are provided with this paper.

References

1. Banani, S. F., Lee, H. O., Hyman, A. A. & Rosen, M. K. Biomolecular condensates: organizers of cellular biochemistry. *Nat. Rev. Mol. Cell Biol.* **18**, 285–298 (2017).
2. Boeynaems, S. et al. Protein phase separation: a new phase in cell biology. *Trends Cell Biol.* **28**, 420–435 (2018).
3. Hirose, T., Ninomiya, K., Nakagawa, S. & Yamazaki, T. A guide to membraneless organelles and their various roles in gene regulation. *Nat. Rev. Mol. Cell Biol.* **24**, 288–304 (2023).
4. Putnam, A., Thomas, L. & Seydoux, G. RNA granules: functional compartments or incidental condensates? *Genes Dev.* **37**, 354–376 (2023).
5. Mittag, T. & Pappu, R. V. A conceptual framework for understanding phase separation and addressing open questions and challenges. *Mol. Cell* **82**, 2201–2214 (2022).
6. Ripin, N. & Parker, R. Formation, function, and pathology of RNP granules. *Cell* **186**, 4737–4756 (2023).
7. Fare, C. M., Villani, A., Drake, L. E. & Shorter, J. Higher-order organization of biomolecular condensates. *Open Biol.* **11**, 210137 (2021).
8. Lafontaine, D. L. J., Riback, J. A., Bascetin, R. & Brangwynne, C. P. The nucleolus as a multiphase liquid condensate. *Nat. Rev. Mol. Cell Biol.* **22**, 165–182 (2021).
9. Riback, J. A. et al. Composition-dependent thermodynamics of intracellular phase separation. *Nature* **581**, 209–214 (2020).
10. Feric, M. et al. Coexisting liquid phases underlie nucleolar sub-compartments. *Cell* **165**, 1686–1697 (2016).
11. Dodson, A. E. & Kennedy, S. Phase separation in germ cells and development. *Dev. Cell* **55**, 4–17 (2020).
12. Voronina, E., Seydoux, G., Sassone-Corsi, P. & Nagamori, I. RNA granules in germ cells. *Cold Spring Harb. Perspect. Biol.* **3**, a002774 (2011).
13. Rangan, P. et al. Temporal and spatial control of germ-plasm RNAs. *Curr. Biol.* **19**, 72–77 (2009).
14. Barckmann, B. et al. Aubergine iCLIP reveals piRNA-dependent decay of mRNAs involved in germ cell development in the early embryo. *Cell Rep.* **12**, 1205–1216 (2015).
15. Lehmann, R. Germ plasm biogenesis—an Oskar-centric perspective. *Curr. Top. Dev. Biol.* **116**, 679–707 (2016).
16. Kistler, K. E. et al. Phase transitioned nuclear Oskar promotes cell division of Drosophila primordial germ cells. *eLife* **7**, e37949 (2018).
17. Trcek, T. et al. Sequence-independent self-assembly of germ granule mRNAs into homotypic clusters. *Mol. Cell* **78**, 941–950.e12 (2020).
18. Trcek, T. et al. Drosophila germ granules are structured and contain homotypic mRNA clusters. *Nat. Commun.* **6**, 7962 (2015).
19. Niepielko, M. G., Eagle, W. V. I. & Gavis, E. R. Stochastic seeding coupled with mRNA self-recruitment generates heterogeneous Drosophila germ granules. *Curr. Biol.* **28**, 1872–1881.e3 (2018).
20. Putnam, A., Cassani, M., Smith, J. & Seydoux, G. A gel phase promotes condensation of liquid P granules in Caenorhabditis elegans embryos. *Nat. Struct. Mol. Biol.* **26**, 220–226 (2019).
21. Roovers, E. F. et al. Tdrd6a regulates the aggregation of Buc into functional subcellular compartments that drive germ cell specification. *Dev. Cell* **46**, 285–301.e9 (2018).
22. Lee, C.-Y. S. et al. Recruitment of mRNAs to P granules by condensation with intrinsically-disordered proteins. *eLife* **9**, e52896 (2020).
23. Cassani, M. & Seydoux, G. Specialized germline P-bodies are required to specify germ cell fate in *Caenorhabditis elegans* embryos. *Development* **149**, dev200920 (2022).
24. Mahowald, A. P. Fine structure of pole cells and polar granules in Drosophila melanogaster. *J. Exp. Zool.* **151**, 201–215 (1962).
25. Mahowald, A. P. Polar granules of Drosophila. II. Ultrastructural changes during early embryogenesis. *J. Exp. Zool.* **167**, 237–261 (1968).
26. Arkov, A. L., Wang, J.-Y. S., Ramos, A. & Lehmann, R. The role of Tudor domains in germline development and polar granule architecture. *Development* **133**, 4053–4062 (2006).
27. Dufourt, J. et al. piRNAs and Aubergine cooperate with Wispy poly(A) polymerase to stabilize mRNAs in the germ plasm. *Nat. Commun.* **8**, 1305 (2017).
28. Vourekas, A., Alexiou, P., Vrettos, N., Maragkakis, M. & Mourelatos, Z. Sequence-dependent but not sequence-specific piRNA adhesion traps mRNAs to the germ plasm. *Nature* **531**, 390–394 (2016).
29. Klattenhoff, C. et al. Drosophila rasiRNA pathway mutations disrupt embryonic axis specification through activation of an ATR/Chk2 DNA damage response. *Dev. Cell* **12**, 45–55 (2007).
30. Wilson, J. E., Connell, J. E. & Macdonald, P. M. *aubergine* enhances *oskar* translation in the *Drosophila* ovary. *Development* **122**, 1631–1639 (1996).
31. Yan, X., Hoek, T. A., Vale, R. D. & Tanenbaum, M. E. Dynamics of translation of single mRNA molecules in vivo. *Cell* **165**, 976–989 (2016).
32. Wang, C., Han, B., Zhou, R. & Zhuang, X. Real-time imaging of translation on single mRNA transcripts in live cells. *Cell* **165**, 990–1001 (2016).
33. Morisaki, T. et al. Real-time quantification of single RNA translation dynamics in living cells. *Science* **352**, 1425–1429 (2016).
34. Pichon, X. et al. Visualization of single endogenous polysomes reveals the dynamics of translation in live human cells. *J. Cell Biol.* **214**, 769–781 (2016).
35. Wu, B., Eliscovich, C., Yoon, Y. J. & Singer, R. H. Translation dynamics of single mRNAs in live cells and neurons. *Science* **352**, 1430–1435 (2016).
36. Bertrand, E. et al. Localization of ASH1 mRNA particles in living yeast. *Mol. Cell* **2**, 437–445 (1998).

37. Raj, A., Van Den Bogaard, P., Rifkin, S. A., Van Oudenaarden, A. & Tyagi, S. Imaging individual mRNA molecules using multiple singly labeled probes. *Nat. Methods* **5**, 877–879 (2008).

38. Dahanukar, A. & Wharton, R. P. The Nanos gradient in Drosophila embryos is generated by translational regulation. *Genes Dev.* **10**, 2610–2621 (1996).

39. Bergsten, S. E. & Gavis, E. R. Role for mRNA localization in translational activation but not spatial restriction of *nanos* RNA. *Development* **126**, 659–669 (1999).

40. Dufourt, J. et al. Imaging translation dynamics in live embryos reveals spatial heterogeneities. *Science* **372**, 840–844 (2021).

41. Mueller, F. et al. FISH-quant: automatic counting of transcripts in 3D FISH images. *Nat. Methods* **10**, 277–278 (2013).

42. Little, S. C., Sinsimer, K. S., Lee, J. J., Wieschaus, E. F. & Gavis, E. R. Independent and coordinate trafficking of single Drosophila germ plasm mRNAs. *Nat. Cell Biol.* **17**, 558–568 (2015).

43. Ramat, A. et al. The PIWI protein Aubergine recruits eIF3 to activate translation in the germ plasm. *Cell Res.* **30**, 421–435 (2020).

44. Götze, M. et al. Translational repression of the *Drosophila nanos* mRNA involves the RNA helicase Belle and RNA coating by Me31B and Trailer hitch. *RNA* **23**, 1552–1568 (2017).

45. Zaessinger, S., Busseau, I. & Simonelig, M. Oskar allows *nanos* mRNA translation in *Drosophila* embryos by preventing its dead-enylation by Smaug/CCR4. *Development* **133**, 4573–4583 (2006).

46. Kubíková, J., Ubartaitė, G., Metz, J. & Jeske, M. Structural basis for binding of *Drosophila* Smaug to the GPCR Smoothened and to the germline inducer Oskar. *Proc. Natl Acad. Sci. Usa.* **120**, e2304385120 (2023).

47. Thomson, T., Liu, N., Arkov, A., Lehmann, R. & Lasko, P. Isolation of new polar granule components in Drosophila reveals P body and ER associated proteins. *Mech. Dev.* **125**, 865–873 (2008).

48. Hakes, A. C. & Gavis, E. R. Plasticity of Drosophila germ granules during germ cell development. *PLoS Biol.* **21**, e3002069 (2023).

49. Jongens, T. A., Hay, B., Jan, L. Y. & Jan, Y. N. The germ cell-less gene product: a posteriorly localized component necessary for germ cell development in Drosophila. *Cell* **70**, 569–584 (1992).

50. Dalby, B. & Glover, D. M. Discrete sequence elements control posterior pole accumulation and translational repression of maternal cyclin B RNA in Drosophila. *EMBO J.* **12**, 1219–1227 (1993).

51. Eichhorn, S. W. et al. mRNA poly(A)-tail changes specified by deadenylation broadly reshape translation in Drosophila oocytes and early embryos. *eLife* **5**, e16955 (2016).

52. Kronja, I. et al. Widespread changes in the posttranscriptional landscape at the drosophila oocyte-to-embryo transition. *Cell Rep.* **7**, 1495–1508 (2014).

53. Hara, M. et al. Identification of PNG kinase substrates uncovers interactions with the translational repressor TRAL in the oocyte-to-embryo transition. *eLife* **7**, e33150 (2018).

54. Adivarahan, S. et al. Spatial organization of single mRNPs at different stages of the gene expression pathway. *Mol. Cell* **72**, 727–738.e5 (2018).

55. Forrest, K. M., Clark, I. E., Jain, R. A. & Gavis, E. R. Temporal complexity within a translational control element in the *nanos* mRNA. *Development* **131**, 5849–5857 (2004).

56. Bracha, D. et al. Mapping local and global liquid phase behavior in living cells using photo-oligomerizable seeds. *Cell* **175**, 1467–1480.e13 (2018).

57. Kirino, Y. et al. Arginine methylation of Piwi proteins catalysed by dPRMT5 is required for Ago3 and Aub stability. *Nat. Cell Biol.* **11**, 652–658 (2009).

58. Nishida, K. M. et al. Functional involvement of Tudor and dPRMT5 in the piRNA processing pathway in Drosophila germlines. *EMBO J.* **28**, 3820–3831 (2009).

59. Kirino, Y. et al. Arginine methylation of Aubergine mediates Tudor binding and germ plasm localization. *RNA* **16**, 70–78 (2010).

60. Vo, H. D. L. et al. Protein components of ribonucleoprotein granules from Drosophila germ cells oligomerize and show distinct spatial organization during germline development. *Sci. Rep.* **9**, 19190 (2019).

61. Johnstone, O. & Lasko, P. Interaction with eIF5B is essential for Vasa function during development. *Development* **131**, 4167–4178 (2004).

62. Eichler, C. E., Hakes, A. C., Hull, B. & Gavis, E. R. Compartmentalized oskar degradation in the germ plasm safeguards germline development. *eLife* **9**, e49988 (2020).

63. Mateju, D. et al. Single-molecule imaging reveals translation of mRNAs Localized to Stress Granules. *Cell* **183**, 1801–1812.e13 (2020).

64. Moon, S. L. et al. Multicolour single-molecule tracking of mRNA interactions with RNP granules. *Nat. Cell Biol.* **21**, 162–168 (2019).

65. Kang, J.-Y. et al. LLPS of FXR1 drives spermiogenesis by activating translation of stored mRNAs. *Science* **377**, eabj6647 (2022).

66. Westerich, K. J. et al. Spatial organization and function of RNA molecules within phase-separated condensates in zebrafish are controlled by Dnd1. *Dev. Cell* **58**, 1578–1592.e5 (2023).

67. Chen, R., Stainier, W., Dufourt, J., Lagha, M. & Lehmann, R. Direct observation of translational activation by a ribonucleoprotein granule. *Nat. Cell Biol.* https://doi.org/10.1038/s41556-024-01452-5 (2024).

68. Dai, P. et al. A translation-activating function of MIWI/piRNA during mouse spermiogenesis. *Cell* **179**, 1566–1581.e16 (2019).

69. Harris, A. N. & Macdonald, P. M. *aubergine* encodes a *Drosophila* polar granule component required for pole cell formation and related to eIF2C. *Development* **128**, 2823–2832 (2001).

70. Rørth, P. Gal4 in the Drosophila female germline. *Mech. Dev.* **78**, 113–118 (1998).

71. Hurd, T. R. et al. Long Oskar controls mitochondrial inheritance in Drosophila melanogaster. *Dev. Cell* **39**, 560–571 (2016).

72. Kina, H., Yoshitani, T., Hanyu-Nakamura, K. & Nakamura, A. Rapid and efficient generation of GFP -knocked-in *Drosophila* by the CRISPR -Cas9-mediated genome editing. *Dev. Growth Differ* **61**, 265–275 (2019).

73. Forrest, K. M. & Gavis, E. R. Live imaging of endogenous RNA reveals a diffusion and entrapment mechanism for nanos mRNA localization in Drosophila. *Curr. Biol.* **13**, 1159–1168 (2003).

74. Murata, Y. & Wharton, R. P. Binding of pumilio to maternal hunch-back mRNA is required for posterior patterning in drosophila embryos. *Cell* **80**, 747–756 (1995).

75. Buszczak, M. et al. The Carnegie protein trap library: a versatile tool for drosophila developmental studies. *Genetics* **175**, 1505–1531 (2007).

76. Shamanski, F. L. & Orr-Weaver, T. L. The Drosophila plutonium and pan gu genes regulate entry into S phase at fertilization. *Cell* **66**, 1289–1300 (1991).

77. Rouget, C. et al. Maternal mRNA deadenylation and decay by the piRNA pathway in the early Drosophila embryo. *Nature* **467**, 1128–1132 (2010).

78. Gunawardane, L. S. et al. A slicer-mediated mechanism for repeat-associated siRNA 5' end formation in *Drosophila*. *Science* **315**, 1587–1590 (2007).

79. Temme, C., Zaessinger, S., Meyer, S., Simonelig, M. & Wahle, E. A complex containing the CCR4 and CAF1 proteins is involved in mRNA deadenylation in Drosophila. *EMBO J.* **23**, 2862–2871 (2004).

80. Verrotti, A. C. & Wharton, R. P. Nanos interacts with Cup in the female germline of *Drosophila*. *Development* **127**, 5225–5232 (2000).

81. Nakamura, A., Amikura, R., Hanyu, K. & Kobayashi, S. Me31B silences translation of oocyte-localizing RNAs through the formation of cytoplasmic RNP complex during *Drosophila* oogenesis. *Development* **128**, 3233–3242 (2001).

82. Chartier, A. et al. Mitochondrial dysfunction reveals the role of mRNA Poly(A) tail regulation in oculopharyngeal muscular dystrophy pathogenesis. *PLoS Genet* **11**, e1005092 (2015).

83. Thomson, T. & Lasko, P. Drosophila Tudor is essential for polar granule assembly and pole cell specification, but not for posterior patterning. *Genesis* **40**, 164–170 (2004).

84. Abbaszadeh, E. K. & Gavis, E. R. Fixed and live visualization of RNAs in Drosophila oocytes and embryos. *Methods* **98**, 34–41 (2016).

85. Schmidt, U. et al. Real-time imaging of cotranscriptional splicing reveals a kinetic model that reduces noise: implications for alternative splicing regulation. *J. Cell Biol.* **193**, 819–829 (2011).

86. Schulman, V. K., Folker, E. S. & Baylies, M. K. A method for reversible drug delivery to internal tissues of *Drosophila* embryos. *Fly* **7**, 193–203 (2013).

87. Jahr, W., Velicky, P. & Danzl, J. G. Strategies to maximize performance in STimulated Emission Depletion (STED) nanoscopy of biological specimens. *Methods* **174**, 27–41 (2020).

88. Ball, G. et al. SIMcheck: a toolbox for successful super-resolution structured illumination microscopy. *Sci. Rep.* **5**, 15915 (2015).

89. Bahry, E. et al. RS-FISH: precise, interactive, fast, and scalable FISH spot detection. *Nat. Methods* **19**, 1563–1567 (2022).

90. Sharma, V. P. et al. Live tumor imaging shows macrophage induction and TMEM-mediated enrichment of cancer stem cells during metastatic dissemination. *Nat. Commun.* **12**, 7300 (2021).

Acknowledgements

Author contributions

Conceptualization: A.R., M.S. Methodology: A.H., A.R., M.S. Investigation: A.H., A.R., C.G. Visualization: A.H., A.R., C.G. Funding acquisition: M.S. Project administration: M.S. Supervision: M.S. Writing—original draft: A.R., M.S. Writing—review & editing: A.R., M.S.

Competing interests

The authors declare no competing interests.

Ethics approval

We support inclusive, diverse, and ethical conduct in research.

Additional information

Supplementary information The online version contains supplementary material available at https://doi.org/10.1038/s41467-024-52346-x.

Correspondence and requests for materials should be addressed to Anne Ramat or Martine Simonelig.

Peer review information *Nature Communications* thanks the anonymous reviewers for their contribution to the peer review of this work. A peer review file is available.

Reprints and permissions information is available at http://www.nature.com/reprints

Publisher's note Springer Nature remains neutral with regard to jurisdictional claims in published maps and institutional affiliations.